Closed-loop Control of Meltpool Temperature in Directed Energy Deposition

Ziyad Smoqi[1*], Benjamin D. Bevans[1], Aniruddha Gaikwad[1], James Craig[2], Alan Abul-Haj[3], Brent Roeder[4], Bill Macy[5], Jeffrey E. Shield[1], Prahalada Rao[1]

[1]Mechanical and Materials Engineering, University of Nebraska-Lincoln, Lincoln, NE; [2]Stratonics, Inc., Lake Forest, CA; [3]ARA Engineering, Sedona, AZ; [4]R3 Digital Sciences, Blacksburg, VA; [5]Macy Consulting, St. Louis, MO.

**Corresponding author, email: zsmoqi@huskers.unl.edu*

Abstract

The objective of this work is to mitigate flaw formation in powder and laser-based directed energy deposition (DED) additive manufacturing process through close-loop control of the meltpool temperature. In this work, the meltpool temperature was controlled by modulating the laser power based on feedback signals from a coaxial two-wavelength imaging pyrometer. The utility of closed-loop control in DED is demonstrated in the context of practically inspired trapezoid-shaped stainless-steel parts (SS 316L). We demonstrate that parts built under closed-loop control have reduced variation in porosity and uniform microstructure compared to parts built under open-loop conditions. For example, post-process characterization showed that closed-loop processed parts had a volume percent porosity ranging from 0.036% to 0.043%. In comparison, open-loop processed parts had a larger variation in volume percent porosity ranging from 0.032% to 0.068%. Further, parts built with closed-loop processing depicted consistent dendritic microstructure. By contrast, parts built with open-loop processing showed microstructure heterogeneity with the presence of both dendritic and planar grains, which in turn translated to large variation in microhardness.

Keywords *Directed Energy Deposition; Closed-loop Control; Meltpool Temperature; Dual-wavelength Pyrometer; Microstructure; Porosity.*

1 Introduction

1.1 Background and Motivation

In the directed energy deposition (DED) process, exemplified in Figure 1, metal powder is sprayed via nozzles onto a substrate and fused (melted) using energy from a laser. The part is built in three dimensions by relative movement of the substrate and nozzles. The DED process studied in this work uses powder material and laser energy source, it is also termed powder-DED (P-DED) or laser-DED (L-DED), and popularly known as Laser Engineered Net Shaping (LENS, a trademark of Optomec). Other embodiments of the process use material in wire form – termed wire-DED – or different energy sources such as an electron beam or an electric arc [1, 2].

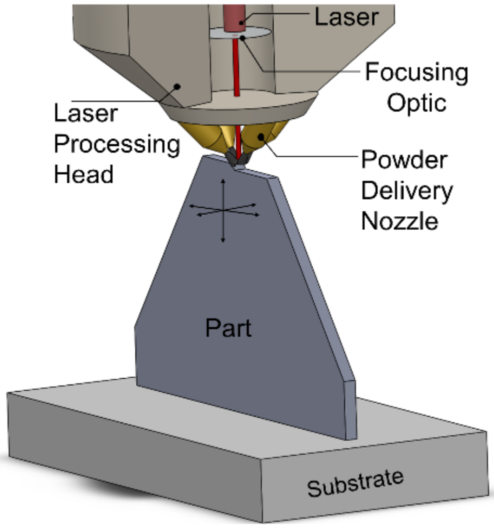

Figure 1: Schematic of the P-DED process. Material in the form of metal powder is sprayed from the sides by four nozzles and fused onto a substrate by energy from a coaxial laser beam.

The DED process provides a new avenue for rapid repair of damaged parts, refurbishment of legacy components, addition of complex features to stock materials, and re-engineering (enhancement) of existing parts with protective coatings [3, 4]. However, the process has a tendency to create flaws, such as porosity and non-uniform (heterogeneous) microstructure [5, 6]. The resulting uncertainty in the part structure leads to large variation in its properties [7]. Hence, despite significant cost and time-to-service advantages, given its lack of consistency, safety-critical industries, such as aerospace and defense, are reticent in adopting the DED process.

Many researchers have highlighted the lack of repeatability of parts produced by additive manufacturing, especially DED, which has hindered its use in large scale production [8-12]. The main cause of flaw formation in DED is linked to the temperature distribution in the part as it is being deposited [13-16]. The temperature distribution is related to the multi-scale thermal aspects of the process and is a function of the part geometry, material properties, and the processing parameters; such as the laser power, scanning velocity and pattern, dwell time between layers, and others [17-20]. For example, at the macro-scale part-level (> 1mm), the uneven distribution of temperature in the part as it is being deposited may lead to severe thermal-induced residual stresses resulting in distortion and cracking [16].

At the meltpool-level, (i.e., the laser-powder interface, < 500 μm) complex thermal, material, and gas flow-related phenomena interact to influence pore formation, inter-granular cracking, and microstructure-level inconsistencies [21-23]. Small disturbances (stochastic variations) in the complex process-machine-material interactions in DED are liable to cause flaw formation [24]. Some common stochastic causes for flaw formation in DED are disturbance in the flow of powder; anomalies in the powder feedstock material, such as contaminants; variation in shape and size of particles; and faults in the machine, such as laser focus aberrations and motion control error leading to uneven deposition of layers [25].

An example of a flaw formation caused due to stochasticity in DED is exemplified in Figure 2. X-ray computed tomography images of two DED parts built under identical processing conditions are shown in Figure 2(a and b) and Figure 2(c and d). The part in Figure 2(a and b) has near ideal geometric accuracy, and only few and small pores. In contrast the part shown in Figure

2(c and d) depicts poor geometric accuracy characterized with a wavy edge, poor surface finish, and large lack-of-fusion pores in the interior of the part exceeding 200 μm in diameter. Therefore, to mitigate the deleterious effect of flaw formation and microstructure heterogeneity in DED, in-process sensor-based monitoring and closed-loop control is being actively researched [26-29].

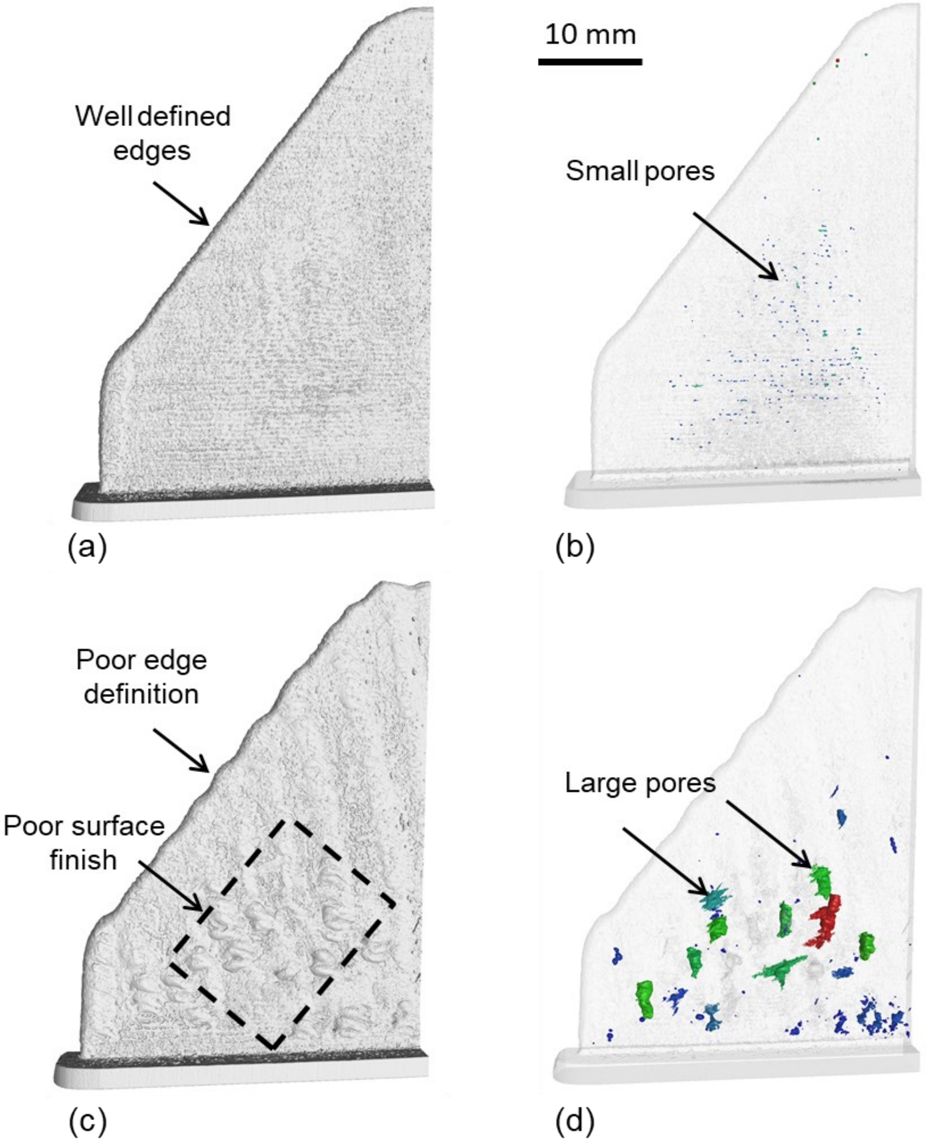

Figure 2: An example of stochastic flaw formation in DED. X-ray CT scans of two stainless steel parts produced under identical DED processing conditions ($P= 325$ W, $V= 8.5$ mm$\cdot$s^{-1}). The part in (a) and (b) depicts near ideal surface finish and few, small pores. The part in (c) and (d) shows poor surface finish, degraded geometry, and large pores.

1.2 Prior Work in Closed-Loop Control of DED

A comprehensive survey of closed-loop control in DED is presented by Reutzel and Nassar [30], and Wang *et al.* [31]. The representative works from the literature are summarized in Table 1, herewith we describe a select few in detail.

Song et al. [32] used an off-axis two-color pyrometer and three high-speed cameras through a rule-based hybrid controller to improve the geometrical accuracy of the build by controlling the laser power. The authors observed that maintaining the meltpool temperature within a specific threshold improved the microstructure as well as the microhardness of the build. Farshidianfar et al. [29] demonstrated closed-loop control of the DED process using an infrared thermal camera in an off-axis configuration and a PID controller. The key idea was to maintain a fixed cooling rate of the part by adjusting the deposition speed. The authors observed significantly less variation in grain size and thereupon microhardness for parts produced under closed-loop conditions as opposed to that of the open-loop conditions.

In a similar vein, Tang and Landers [33] used a coaxial non-imaging pyrometer to control the meltpool temperature and track height measurement through a rule-based controller in a layer-by-layer fashion. The control system was implemented by building a single-track multi-layer part, which showed improved geometrical accuracy. The authors underscore the challenges with controlling the meltpool temperature for a multi-hatch, multi-layer part using a single point meltpool temperature value.

Recent commercial DED machines from Optomec are equipped with meltpool imaging cameras, this system can monitor the meltpool shape and intensity but not the temperature. While imaging pyrometers have been incorporated into the laser path of commercial machines, these have not been integrated with a closed-loop control mechanism [34]. For example, the use of 2D imaging pyrometry for flaw monitoring in DED has been demonstrated by Bian *et al.* [35]. Imaging pyrometers have also been used in the context of process monitoring in laser powder bed fusion additive manufacturing by Hooper *et al.* [36], and Jared *et al.* [37].

Table 1: A survey of closed-loop control in DED.

Sensor Type	**Author**	**Configuration**	**Control signal**	**Controlled variable**	**Controller Type**	**Outcome**	**Limitations**
Two-color pyrometer	Salehi and Brandt [38]	Coaxial	Meltpool temperature	Laser power	PID	Minimize the dilution and heat affected zone in clad layer	Single track study
	Song *et al.* [32]	Off-axis	Meltpool temperature	Laser power	Rule-based	Improved geometric accuracy	Single point temperature measurement
Single-wavelength pyrometer	Nassar *et. al.* [39]	Coaxial	Start point temperature	Hatch order	Rule-based	More uniform microstructure and microhardness	Non-imaging Single point temperature measurement
	Tang and Landers [33, 40]	Coaxial	Meltpool temperature	Laser power	Rule-based	Consistent track morphology	Multi-layer, single track study, single point temperature measurement
IR Camera	Farshidian far *et al.* [29]	Off-axis	Part temperature	Scanning speed	PID	Controlled cooling rate, Less variation in grain size/ microhardness	Relative temperature measurement / multi-layer, single track study
	Gibson *et al.* [41]	Coaxial	Meltpool size	Laser power, velocity, and deposition rate	Multiple modalities	Consistent track geometry	Multi-layer, single track study
	Akbari and Kovacevic [28]	Coaxial	Meltpool size	Laser power	PID	Homogeneity of microstructure	Multi-layer, single track study
Optical coherent tomography	Becker *et. al.* [42]	Coaxial	Track height	Wire feed rate	PI	Improved geometric accuracy	Single point measurement

While previous works in the literature have demonstrated the importance of closed-loop control in DED, a key limitation that motivates the need for further research is that closed-loop control has been demonstrated for only parts with a uniform cross-section. Typically, rectangular parts are produced consisting of single hatch per layer and ten layers at most. However, in practical DED applications, multiple hatches of material are deposited in a layer, and over several hundred layers. In other words, closed-loop control in DED has yet to be demonstrated in the context of a complex part with varying cross-section geometries consisting of multiple hatches and layers.

In the current work closed-loop control is demonstrated in the context of a practical trapezoid-shaped part consisting of multiple hatches (4 hatches per layer) and multiple layers (198 layers). The changing cross-section of the test part used in this work presents an additional challenge for closed-loop control in DED. A 2D imaging pyrometer sensing system is used to control the meltpool temperature through automatic modulation of the laser power. The pyrometer is located coaxial to the laser path and provides a line-of-sight 2D temperature map of the meltpool at the sampling rate of 2.5 Hz. Since, the sensor is coaxial to the laser, it is scalable to parts with complex geometries, always in focus, and capable of collecting data over multiple hatches. To the best of the authors' knowledge, this is one of the first works to use coaxial dual-wavelength imaging pyrometry for real-time, closed-loop control of meltpool temperature in the context of a large multi-hatch DED part.

2 Methods

2.1 Test Parts and Experiments

Six trapezoid-shaped parts (Figure 3) were deposited using an Optomec MR7 LENS system. The powder was sprayed from four nozzles carried in a stream of Argon gas, and melted by a Ytterbium fiber laser operating in continuous mode (IPG Photonics, 1070 nm wavelength). The powder (Praxair FE-271-4) used was stainless steel 316L with a particle size ranging between 50-250 µm. Nominal powder composition was Cr 17%, Ni 12%, Mo 2.5%, with base element Fe.

Parts were deposited under two conditions, namely, closed-loop processing and open-loop processing. In open-loop processing, the laser power (P) is maintained constant at 410 W throughout the build, while in closed-loop processing, the laser power (P) is automatically adjusted in the range of 360 W to 550 W to maintain the meltpool temperature at a setpoint of 1650 ± 50°C. Rest of the process conditions are identical for the both processing conditions (Table 2). Further details regarding the closed-loop control scheme are discussed in Sec. 2.4.

The three parts built under closed-loop conditions were labeled as C1, C2, and C3. The parts deposited under open-loop processing conditions were labeled as O1, O2, and O3. As shown in Figure 3, the test part has a tapering width that reduces in size from 83.75 mm (3.3 inch) to 24.6 mm (~ 1 inch) over a build height of 49.5 mm (~ 2 inch). Two test parts were built on each substrate (165 mm × 165 mm × 12.5 mm). There was a cooling time of two hours between each of the two parts printed on the same substrate. The distance between the two samples was ~80 mm. While the thermal mass of the overall part increases after the deposition of the first test part, however, the change is negligible (~ 7,500 mm^3) in comparison with the large thermal mass of the substrate (~340,312.5 mm^3).

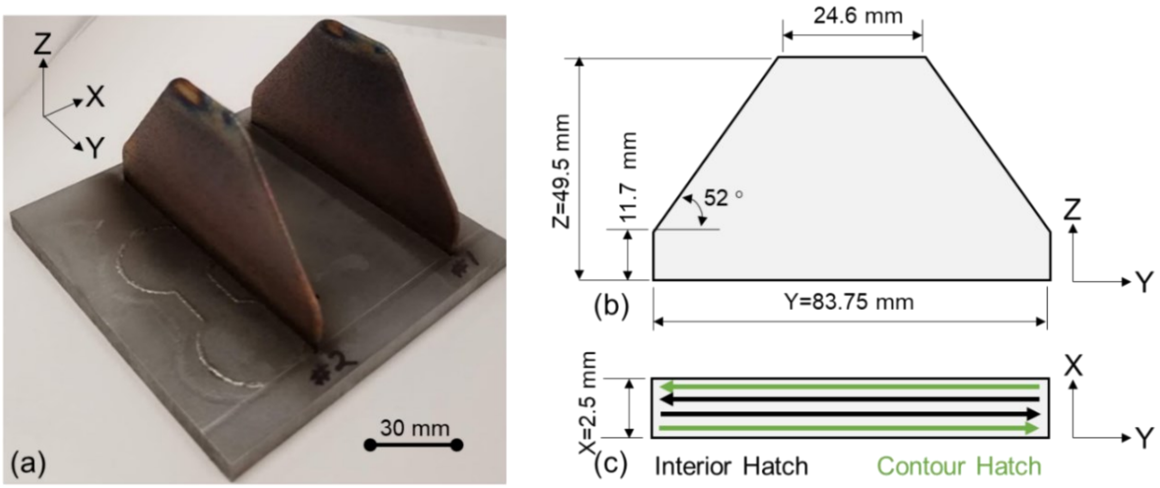

Figure 3: (a) Photograph of as built SS 316L parts used in this work and (b) The dimensions of the trapezoidal parts. (c)The deposition and scan pattern under which the parts are produced. The substrate is stainless steel and 12.7 mm thick. The parts shown in this figure were produced under open-loop processing conditions; burn marks are noted near the top of these parts as a consequence of overheating.

Referring to Figure 3, the width of the part is 2.5 mm (~ 0.1 inch). Each layer is formed from four hatches - two interior and one on each of the outside edges (contour hatch). Hatches were spaced 500 µm (0.02 inch) from each other. The height of each layer (Z-direction) remained constant throughout the build at 250 µm (0.01 inch). A rectilinear hatch pattern that alternates at opposite ends on the part is used. The part consists of 198 layers. No dwell time is programed between hatches or layers, resulting in a build time of 65 minutes per part. Other processing conditions that were held constant are reported in Table 2.

Unlike simple one-hatch thick uniform cross-section rectangular thin-wall shaped test parts, popularly studied in the DED literature in the context of monitoring and closed-loop control [28, 29, 43], the trapezoidal part geometry used in this work creates an additional challenge. The length of the part reduces with the build height, and hence the time between layers also decreases proportionally (as the deposition speed is constant). The change in the cooling rate with the build height is therefore more drastic for the trapezoidal-shaped part used in this work compared to a uniform rectangular thin-wall geometry. The accelerated change in cooling rates is likely to exacerbate microstructure heterogeneity if the laser power is not modulated in real-time to maintain the meltpool temperature. To compound the challenge, the part has multiple hatches − 2 contours and 2 interior hatches − which have distinctive cooling characteristics. The contour hatches are liable to cool faster compared to the interior hatches due to forced convection by argon gas from the nozzle.

Table 2: Processing parameters that were held constant for the DED experiments in this work.

Powder Dispense Rate $[g \cdot s^{-1}]$	Deposition Speed $V[mm \cdot s^{-1}]$	Hatch Spacing H [mm]	Layer Thickness T [mm]	*Stand-off* Distance [mm]
0.1	10.0	0.5	0.25	9.5

2.2 Sensing and Calibration

A two-wavelength imaging pyrometer (ThermaViz by Stratonics, Inc.) is used in this work to capture the meltpool image in both open-loop and closed-loop processing conditions [37]. The ThermaViz imaging pyrometer dimensions are ~150 mm × 150 mm × 75 mm. The pyrometer was integrated into a co-axial configuration with the laser, forming a direct line of sight of the meltpool. Therefore, the meltpool is always in the field of view of the instrument. The pyrometer resolves the temperature over a 752 pixel × 480 pixel region, with a resolution of 11 µm per pixel.

The pyrometer measures the meltpool temperature at two different wavelengths, namely, 750 nm and 900 nm. The measurement obtained is an approximate temperature map of the meltpool due to the change in emissivity. The key aspect of the pyrometer is the measurement of the meltpool temperature at two wavelengths independently of emissivity, which provides a more accurate temperature measurement than a single-wavelength pyrometer [44]. The accuracy of temperature measurement is typically within ±5°C [45]. To explain further, when an object is heated, it emits electromagnetic radiation across different wavelengths governed by Planck's law

[36, 46]. The intensity of the radiation is a function of the temperature of the body, the particular wavelength at which the radiation is measured, and thermal emissivity of the body. The thermal emissivity is not constant but is dependent on the surface characteristics of the object being measured, its temperature, and angle at which the surface is measured [46].

The pyrometer readings are calibrated using an incandescent tungsten lamp with a known temperature response. The diameter of the lamp is 10 mm and its length is 20 mm (Figure 4(a)). A calibration kit equipped with the tungsten lamp, power supply source, calibration certificate, documentation and software for automatic calibration is provided by Stratonics with these sensor array. The calibration procedure, which is widely used in practice, involves placing the tungsten incandescent lamp in the DED machine and positioning it at the point where the meltpool is formed, i.e., along the laser axis and below the laser delivery tube [47].

The validity of the calibration procedure is explained in the context of Figure 4(b), which shows a representative meltpool thermal image ranging from 1600 to 2600 K (1327 to 2327°C) for titanium alloy Ti6Al4V (melting point 1938 K, 1664°C). The inner region of the meltpool is liquid phase and the outer region is solid phase. The boundary between the two regions is marked by a smooth contour. The outer regions of the meltpool, viz., in the solid phase transitions into a region with un-melted powder particles. Similar contours are observed in the meltpool images obtained in this work (Figure 6)

Referring to the color scale, the light blue color corresponds to temperature readings between 1850-1900 K (1577 - 1627°C), and the light green color just across the purple melting contour, corresponds to 2000 to 2050 K (1727 -1777 °C). These light blue and green colors encompass the melting temperature of titanium 1938 K (1664°C). The average temperature over the light blue and green region is 1950 K (~ 1677°C), viz., near the melting temperature of Ti6Al4V (1938 K).

The liquid phase and solid phase demarcations captured by the pyrometer are correlated with the physics of the process and thus substantiate the viability of the calibration and measurements of the pyrometer. These temperature boundaries also carry over to the meltpool of SS 316L as will be demonstrated in the context of Figure 6 in Sec. 2.3.

Next, using this tungsten lamp the pyrometer was calibrated in the temperature range from 1400 to 2500°C in steps of 100°C. The calibration curve is shown in Figure 5. This calibration curve is used to translate the radiant intensity captured by the pyrometer to a temperature reading. On the y-axis of Figure 5 is the temperature of the incandescent tungsten lamp. On the x-axis is the ratio of the radiant intensity measured by the dual wavelength imaging pyrometer at 750 nm and 900 nm. From this calibration curve an intensity measurement at each pixel recorded by the imaging pyrometer is readily converted to a temperature measurement.

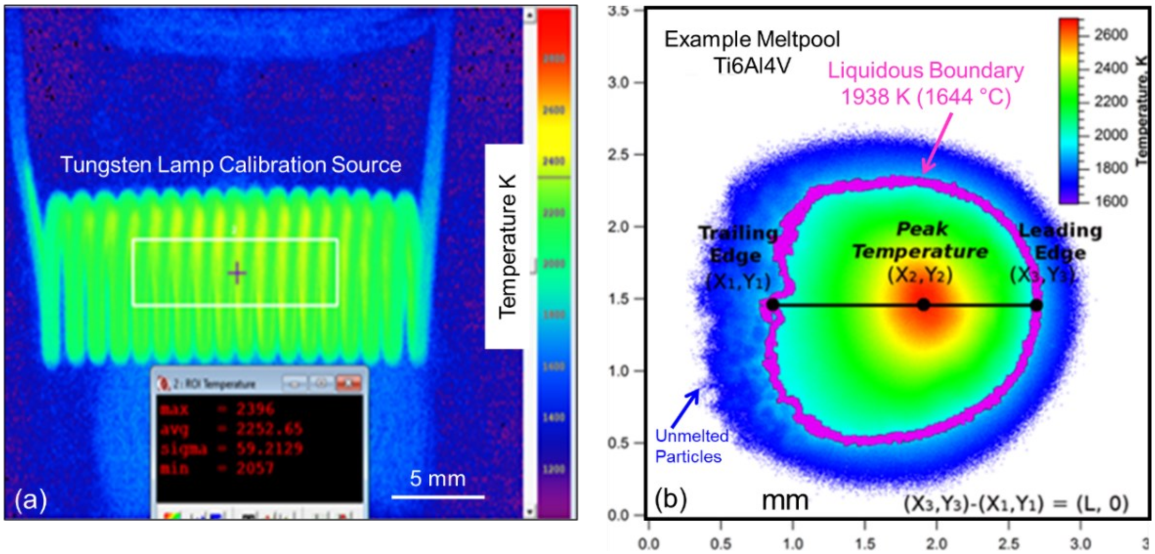

```
max   = 2396
avg   = 2252.65
sigma = 59.2129
min   = 2057
```

Figure 4: (a) Calibration with a tungsten incandescent lamp. (b) Representative thermal image of a meltpool during DED of titanium alloy material. The color scale temperature ranges from 1600 to 2600 K (1327 to 2327°C). A smooth boundary (purple line) separates the solidus and liquidus region of 1938 K. Un-melted particles are observed along the trailing edge.

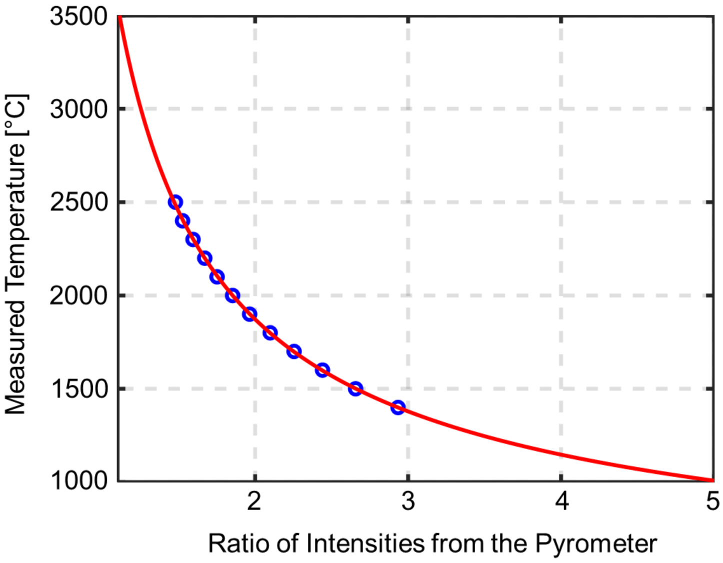

Figure 5: The calibration curve for the pyrometer with respect to a known incandescent source (tungsten lamp). On the x-axis are the ratio of the radiant intensity observed at 750 nm and 900 nm. On the y-axis is the temperature observed from a known incandescent light source. The blue dots are the experimental data points obtained during calibration; the red line is the best fitted curve.

2.3 Data Acquisition and Meltpool Signatures

At the recorded frame rate of 2.5 Hz, approximately 10,000 meltpool images are acquired for each part. The selected sampling rate is because the goal of this work was to perform hatch-by-hatch meltpool temperature control as opposed to localized high-resolution temperature control. Furthermore, the pyrometer used in this work provides a 2D areal (113 µm × 113 µm) temperature distribution of the meltpool as opposed to a single point temperature in prior work [33, 39, 40, 42]. Therefore, the sampling rate of 2.5 Hz is deemed to be sufficient.

Although the sampling rate for the pyrometer can be increased beyond 1 kHz, however, a higher sampling rate would require increased data buffering, storage, transfer, and computation requirements. Hence, in this work there is a tradeoff between sensor sampling rate and tractability of the controller system. However, a higher sampling rate would be essential if the scanning velocity were to increase beyond the 10 mm/s used in this work.

Each meltpool image is synchronized with its corresponding laser power and build position. A representative meltpool image acquired from the two-wavelength pyrometer is shown in Figure 6(a). The meltpool image in Figure 6(a) is further stratified into two regions, namely, the meltpool region and the annulus region. This demarcation is shown graphically for a pyrometer image in Figure 6(b) and (c), respectively.

The meltpool region, Figure 6(b), corresponds to the location of every pixel in the pyrometer image whose temperature is greater than 1371°C (melting point of SS 316). Similarly, the annulus region of the meltpool, Figure 6(c), corresponds to the location of each pixel in the pyrometer image that reads between 1000°C and 1371°C. These thresholds were chosen as they result in distinctive boundaries demarcating solidus and liquidus regions of the meltpool for SS 316L akin to Figure 4.

Figure 6(d), shows a spatial sampling of the temperature profile across the meltpool from a 200 pixel × 10 pixel (2 mm × 0.11 mm) demarcated in Figure 6(a). This 1D temperature profile reveals that the peak meltpool temperature encompasses a small area in the center of the meltpool, and the temperature decreases rapidly from the center. For each meltpool region identified from the pyrometer image we extract and record the following process signatures: (i) peak (maximum) meltpool temperature, (ii) average meltpool temperature, (iii) standard deviation of meltpool temperature, and (iv) meltpool area. Similar metrics were recorded for the annulus region of the meltpool.

We note that when measuring temperature of a meltpool pixel-by-pixel, the measured temperature may fluctuate more than the native precision of the calibration due to natural variation in the process, and interference from spatter and soot in the meltpool region. Hence, the pixel-to-pixel variation can be often as large as 100°C. Therefore, instead of measuring temperature over single pixels for process control, we spatially average the peak temperature over 10 pixels × 10 pixels (0.0121 mm^2), as well as temporally over multiple consecutive meltpool images. The procedure, which is explained in the forthcoming Sec. 2.4 (closed-loop controller), mitigates the deleterious effect of local variations in the meltpool temperature.

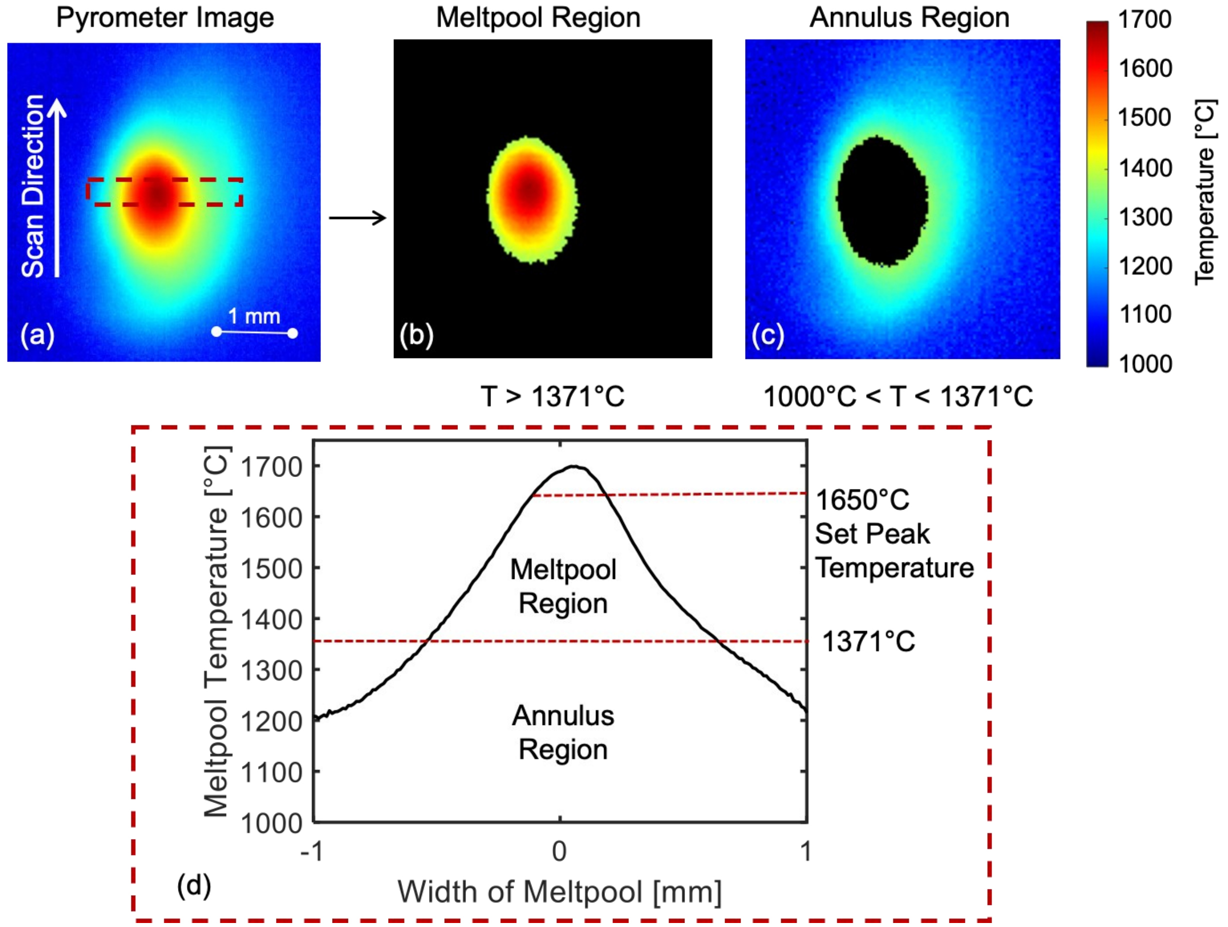

Figure 6: (a) The as-received pyrometer image of the meltpool, which is stratified into meltpool and annulus regions for correlating the meltpool behavior with microstructure evolution and porosity formation. (b) The meltpool region consists of pixels over 1371°C (melting point of SS 316L) (c) The annulus region consists of pixels with the recorded temperature in the range of 1000 to 1371°C. (d) A 1-D perspective of the meltpool image obtained by sampling of the temperature of the annotated pixels through the center of the meltpool image. The sampled area in (a) is ~200 pixels long and 10 pixels wide, corresponding to 2 mm and 0.11 mm, respectively.

2.4 Closed-loop Process Control

A rule-based closed-loop control scheme is used in this work to maintain the meltpool temperature. The schematic of the closed-loop control system is shown in Figure 7, and the control logic is summarized in Figure 8. The laser power and position were synchronized with the pyrometer data and logged in the closed-loop control system at 2.5 Hz. This allowed the meltpool temperature to be correlated to specific positions along the laser path. The peak meltpool temperature is controlled by adjusting the laser power with respect to the difference between the measured and set point temperature (1650°C), as will be described shortly.

The meltpool temperature was averaged in a small area encompassing the center of the meltpool corresponding to 0.0121 mm^2 (10 pixels × 10 pixels, 113 µm × 113 µm) physical size, from every image frame obtained from the pyrometer. As described previously in Sec. 2.3, this spatially averaged meltpool temperature is termed as the *peak meltpool temperature.*

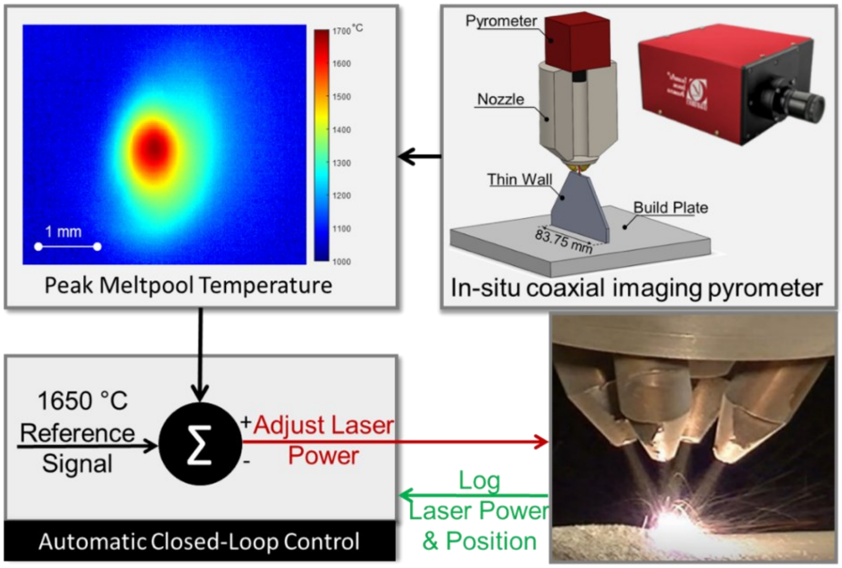

Figure 7: Control-Loop used to maintain the peak meltpool temperature at 1650 ± 50°C using a Stratonics two-wavelength imaging pyrometer and Optomec's Lens MR7 DED machine. The peak meltpool temperature is measured in a 10 pixel × 10 pixel square surrounding the center of the meltpool image. The laser power is adjusted proportional to the peak meltpool temperature. The system logs the position of the nozzle and the adjusted laser power.

The setpoint for the peak meltpool temperature was 1650 ± 50°C (1873 to 1973 K). This setpoint temperature is chosen as it is ~20% higher than the melting temperature of SS 316 of ~1371°C (1644 K) and in agreement with processing parameter levels for the material recommended by the machine tool manufacturer (Optomec). These process parameters and meltpool temperature levels were determined by Optomec based on offline testing and optimization. The meltpool temperature was identified by adjusting power levels and deposition velocity to optimize for time efficiency, component precision, soot formation (a high energy density leads to material vaporization) and to avoid lack of fusion (resulting from low energy density), and for uniform deposition of a track.

When the meltpool peak temperature varied ± 3% outside the 1650°C setpoint range, i.e., 1650 ± 50°C, the laser power level was increased or decreased. This closed-loop control system is designed to maintain a uniform peak meltpool temperature along the processing path and across hatches throughout the build. The controller logic is further explained in the context of Figure 8. The peak meltpool temperature (P_t) was averaged over 16 consecutive trailing meltpool images. The average of the peak meltpool temperature (a_t) of the 16 consecutive images is compared to the setpoint of 1650°C. Next, the error (e_t) between the setpoint temperature of 1650°C and average peak meltpool temperature (a_t) is computed, $e_t = a_t - 1650°C$. If this error (e_t) is greater than +50°C or less than -50°C, the laser power was decreased or increased by 1 Watt accordingly.

An alternative approach is to adjust the laser power as a dynamic function of the error ($e_{t,}$) akin to a PID controller as implemented in Ref. [28, 29, 38]. In contrast, the rule-based control logic implemented in this work is based on simple statistical calculations, which does not need involved data storage, data processing, and tuning of controller parameters, and is potentially material agnostic. Hence, the developed control logic is amenable for implementation onboard the CNC controller of a DED machine.

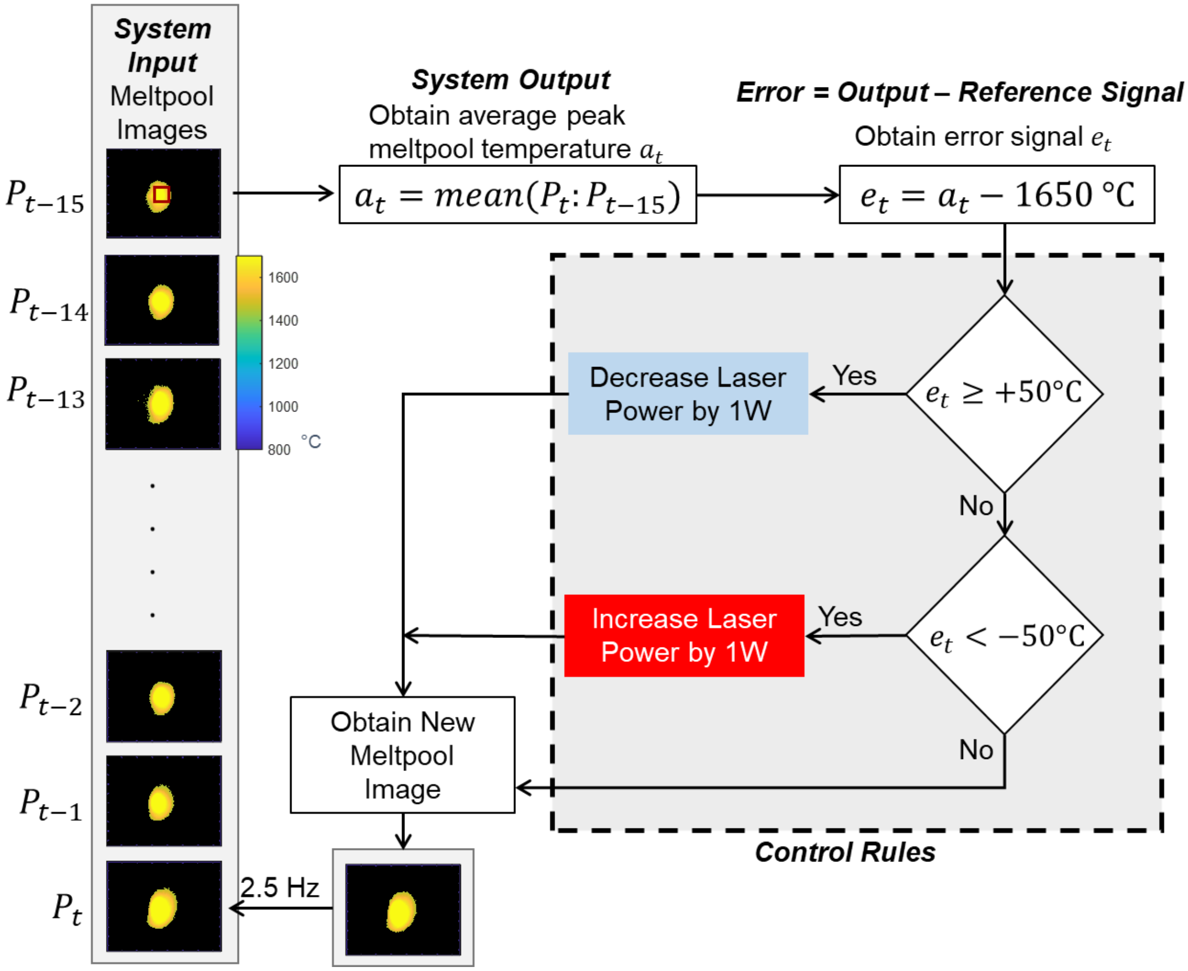

Figure 8: Block diagram of the rule-based controller used to maintain the meltpool at a peak temperature of 1650°C. The average of the peak meltpool temperature (a_t) was taken over a trailing 16 readings. Then the error (e_t) from 1650°C was found and the laser power was adjusted accordingly. Then the new meltpool reading was recorded, repeating at a rate of 2.5 Hz.

The control logic is further detailed herewith; the control logic and parameters are derived based on extensive empirical tuning not reported in this work.

- The meltpool image from the current frame and that of the preceding 15 frames, i.e., 16 total meltpool frames, are used to calculate the average peak meltpool temperature (a_t). Averaging over multiple frames mitigates the effects of stochastic noise and outliers and suppresses the controller from overshooting. Consequently, the controller has a short-term memory that allows it to store and transfer information between hatches. The controller reads and stores the location of the meltpool and laser power from the machine. This allows the controller to track the position of the laser and record its precise location on a particular hatch (interior or contour). Considering a scanning speed of 10 mm/s and sampling time of 0.4s for the pyrometer, the measurement is updated every 4 mm along the hatch. Since the shortest hatch length is ~ 24 mm, the system is updated at least 6 times along the hatch.

- If the error, $e_t = a_t - 1650$°C, exceeds +50°C the laser power was reduced by 1 W from its previous value. Likewise, if the error e_t is less than -50 °C, the laser power is increased by 1 W from its previous value. The dead band region of ± 50 °C ensures that the controller does not react to stochastic errors. The power was changed gradually in steps of 1 W to avoid a sudden change in temperature and thereby avoid large thermal gradients. The control decision (increasing or decreasing the laser power 1 W) was implemented over a frame cycle, e.g., 2.5 Hz. In other words, as long as the error signal e_t was beyond 1650 ± 50°C, the laser power was adjusted frame-by-frame. If the error signal recovered within 1650 ± 50°C, the laser power adjustments were stopped. In this manner, the controller adjusts the laser power level over the entire build, from initial to the final layers, and over all hatches (interior and contour).

As will be described in Sec. 3.1 in the context of Figure 11, this closed-loop control approach maintained the meltpool temperature within 1650 ± 50°C. In contrast, the peak meltpool temperature of parts built using constant laser power of 410 W (Open-loop processing) had a large variation, ranging from 1600 to over 2000°C. As shown in Sec. 3.3 and 3.4, parts processed with closed-loop control showed reduced porosity and homogenous microstructure compared to Open-loop processing.

2.5 Post-process Characterization

Extensive post-process analyses were conducted to compare the physical properties of parts produced under closed-loop and open-loop conditions. These analyses included both non-destructive X-ray computed tomography (XCT) for porosity assessment and destructive metallographic characterization. Destructive analyses encompassed optical and scanning electron microscopy (nature of pore formation and microstructure), energy dispersive X-ray spectroscopy (EDS, material composition) and X-ray diffraction (XRD, microstructure phases).

For ease of post-process analysis, the parts were sectioned across the middle into two 24.75 mm tall samples, labeled A and B using electro-discharge machining. Hereafter, the term samples is used in reference to the two halves of each part. Accordingly, there are two samples per part, for a total of 12 samples (6 parts × 2 samples). Each sample is further demarcated into four sub-sections, measuring ~6.2 mm in height, as shown in Figure 9 (8 sub-sections per part). For a volumetric porosity analysis, X-ray computed tomography (XCT) was performed using a Nikon XTH225 ST system. This analysis was performed at a voxel resolution of 10 µm. The Volume Graphics software (VGSTUDIO MAX 3.4.0) was used for subsequent porosity analysis.

The cross-section faces of these samples that were near the center of the thin wall were polished in progressively smaller steps starting with fixed abrasive 120 grit SiC paper and ending with 1200 grit. The final fine polishing steps were carried out with 3 µm and 1 µm particle size diamond pastes using Dialube Blue lubricant, followed by 0.05 µm alumna slurry. After polishing, optical microscopy was performed to visualize the relative porosity between parts produced under closed-loop and open-loop processing conditions. Thirteen images were taken per sample, resulting in 26 images per part. These optical images were taken so that the top of one image corresponded with the bottom of the following image. This allowed for a complete picture of the cross-section microstructure.

Subsequent to optical microscopy, samples were etched with Adler's reagent for 60 seconds, which revealed the grain structure which was observed using scanning electron microscopy (SEM, Helios 660 NanaoLab from FEI). Eight images were taken for each of the eight sub-sections for the part. These eight images were taken using the pattern shown in Figure 10. Accordingly, 64 SEM images were acquired per part. Further, to correlate the meltpool characteristics described in Sec. 3.1 the part was stratified into the eight sections shown in Figure 9(b) for a one-to-one comparison between the in-process sensor data and the part material characteristics on a meso-scale.

Energy dispersive X-ray spectroscopy (EDS, Octane Super EDAX) was performed to determine the consistency in elemental composition of the microstructure between closed-loop and open-loop processing. The concentrations of three main elements in SS 316L stainless steel (Fe, Cr, and Ni) were measured through EDS analysis at five random points at each of the eight sub-sections along the vertical height shown in Figure 10. Accordingly, there are 40 EDS spot measurements points per part (8 sub-sections × 5 measurements). Apart from EDS spot measurements, EDS line scans were conducted on different types of microstructure from closed-loop- and open-loop-processed parts to ascertain severity of micro-segregation.

Next, X-ray diffraction (XRD) was performed to demarcate differences in material phase between closed-loop- and open-loop-processed parts. For XRD analysis a Rigaku SmartLab diffractometer was used with Cu Kα radiation ($\lambda = 1.5418$ Å). The EDS and XRD studies are important to rule the presence of micro-segregation and phase transformation between closed-loop and open-loop Processed parts.

Vickers microhardness (Vickers, Hv) testing was performed on each part under a load of 500 grams and a dwell time of 10 seconds using a LECO AMH55L Automatic Hardness Tester. Hardness testing was done in accordance with ASTM E384; a minimum distance of 3 times the pyramidal diagonal of the Vickers indenter was maintained between indentations. Two sets of five hardness readings were taken at each of the eight sections shown in Figure 10.

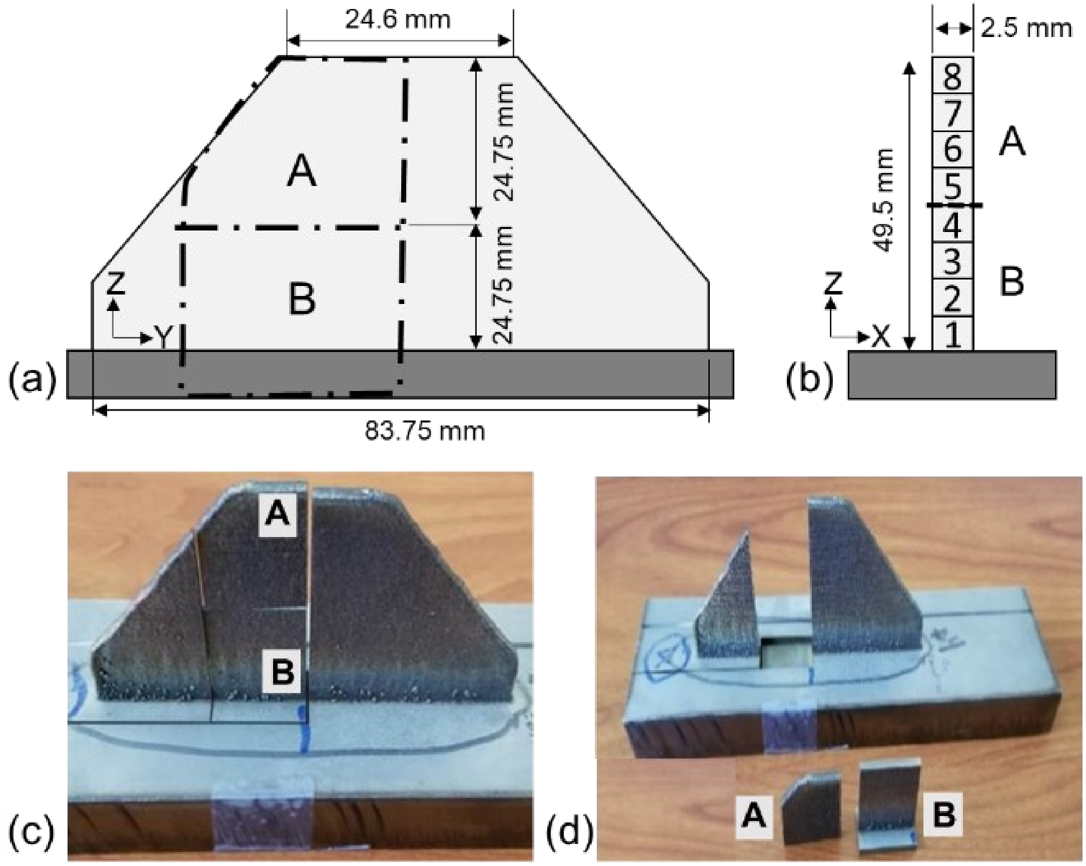

Figure 9: (a and b) Schematic and (c and d) pictures of the part cut into sample A and sample B in order to perform metallurgical analysis. Sample A is the top cross-section and Sample B is the bottom cross-section. The part is divided into 8 sub-sections of 6.2 mm height for analysis.

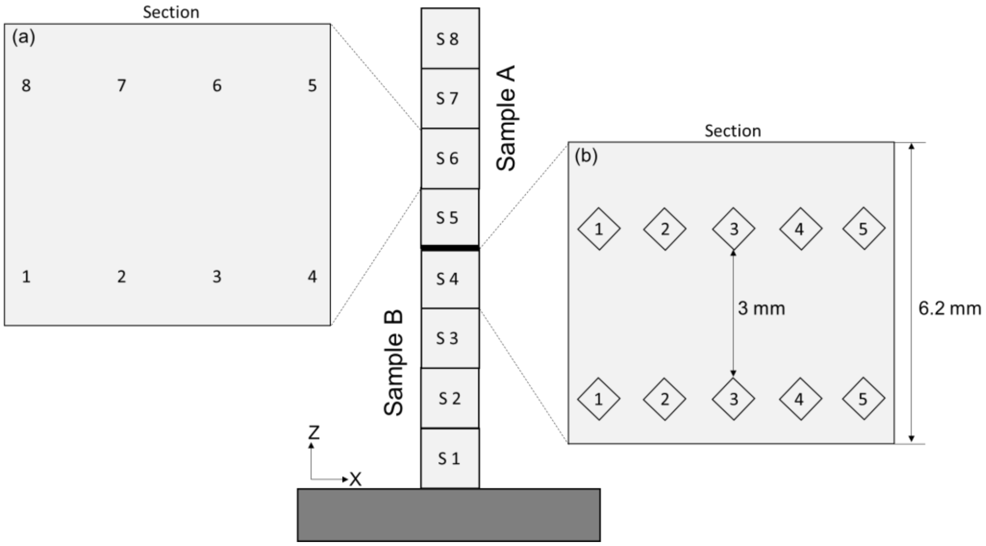

Figure 10: Schematic of a part divided into eight sub-sections, labeled S1 through S8. Each sub-section is 6.2 mm tall and 2.5 mm wide. Schematic of locations (a) where the SEM images were taken to perform grain morphology analysis and (b) where microhardness readings were taken for each sub-section.

3 Results and Discussion

3.1 Effect of Closed-loop Process Control on Meltpool Temperature and Size

The aim of this section is to show the difference in meltpool behavior (temperature and area) resulting from closed-loop and open-loop processing conditions. The following analyses in the context of Figure 11 through Figure 14 compare the meltpool characteristics of open-loop processing with those from closed-loop processing. The results reveal that the meltpool temperature and area of closed-loop processed parts are more consistent across hatches and between layers of the same part, as well as between different parts. As evident in Figure 11, the open-loop processed parts (O1, O2, O3) depict a large variation in peak meltpool temperature both within and between parts, despite maintaining the laser power constant at 410 W.

In the DED process, identical process parameters may lead to different meltpool size and temperature owing to complex conductive, convective, and radiative heat transfer phenomena

[22].The deleterious effect of stochastic disturbances on part quality was emphasized in the context of Figure 2 (Sec. 1.1), where two DED parts built under identical processing conditions differed considerably in porosity, surface finish, and geometric integrity. The effect of stochastic disturbances on the peak meltpool temperature is evident in Figure 11. For example, in the context of the open-loop processed part O1 the peak meltpool temperature ranges from 1600 to 2000 °C, while that of O2 ranges from 1550 to 1700°C. In contrast, the peak meltpool temperature for closed-loop processed parts (C1, C2, C3) is consistently within 1650 ± 50°C for the bulk of the parts.

Thus, there is a considerably larger variation in the meltpool temperature in open-loop processing. This is most likely caused due to highly dynamic heat transfer phenomena and process uncertainty (stochasticity). As explained by Thomson *et al.* [18, 22] small changes in the gas flow rate, and powder deposition rate considerably effect the meltpool temperature. For example, Heigel *et al.* [48] report that the forced convection created by the inert gas flow used to deliver metal powder significantly affects the causal heat transfer mechanisms. Hence, there is a need for closed-loop control of meltpool temperature to limit the variation in meltpool temperature and the tendency of the process for flaw formation, which often occur due to stochastic fluctuations in the process conditions [5, 33, 35].

Figure 12(a) shows the mean temperature of the meltpool region (average temperature of pixels above the melting point of SS 316L, ~1371°C). The mean temperature of the meltpool region for all three closed-loop processed parts are largely steady at 1480 ± 20°C, which is approximately 110°C higher than the melting temperature of SS 316L. By contrast, in case of the three open-loop processed parts, the mean temperature of the meltpool region ranged from 1440 to 1560°C between different parts.

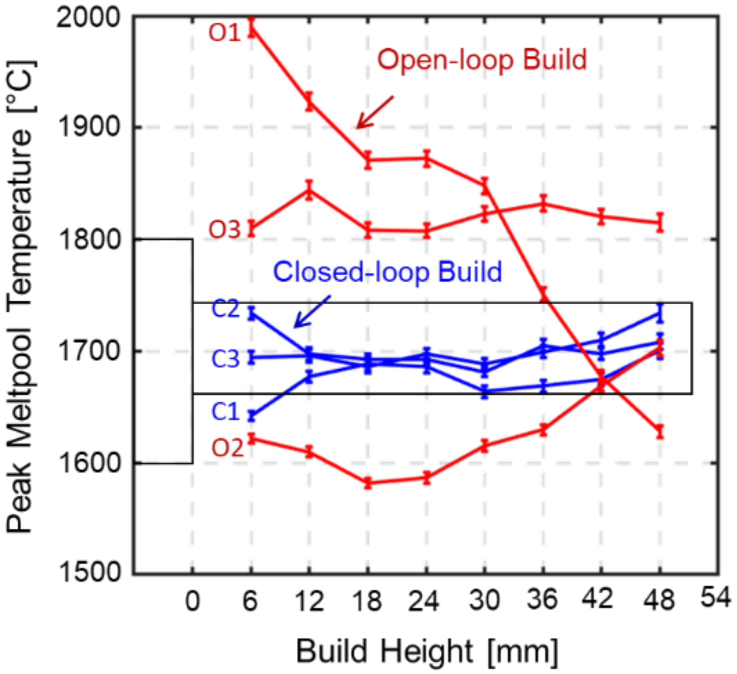

Figure 11: Comparison of the peak meltpool temperature for the open-loop and closed-loop processed parts. The peak meltpool temperature for the parts processed under open-loop conditions (fixed laser power of 410 W) varies from ~ 1560 to 2000°C. In contrast, the peak meltpool temperature for the parts built with closed-loop control of the laser power remains within 1650 ± 50°C. Error bars show the mean ± 1 standard error.

The mean and standard deviation of the mean meltpool temperature data shown in Figure 12(a) corresponding to all the closed-loop processed parts C1, C2, and C3 was estimated to be ~1483°C and ~ 4.70°C, respectively. For open-loop processed parts O1, O2, and O3, the mean and standard deviation of the mean meltpool temperature were ~1494 and ~ 31.81°C, respectively.

The annulus temperature as shown in Figure 12(b), follows a similar steady trend for parts deposited under closed-loop processing conditions, compared to large temperature variation between and within open-loop processed parts. Continuing with the analysis, we stratified the mean temperature of the meltpool region by its hatch location on a layer, i.e., contour and interior hatches. Shown in Figure 12(c) and (d) is the mean temperature of the meltpool region for the interior and contour hatches for the closed-loop and open-loop processed parts, respectively. In comparison to the closed-loop processed parts, there is a relatively larger variation in the temperature of the meltpool region from the interior and contour hatches for open-loop processed parts. This result underscores the importance of adjusting the laser power within a layer, across hatches, as opposed to at the end of the layer because, the meltpool temperature varies greatly between contour and interior hatches. An off-axis sensing system would not be capable of adjusting the process hatch-by-hatch.

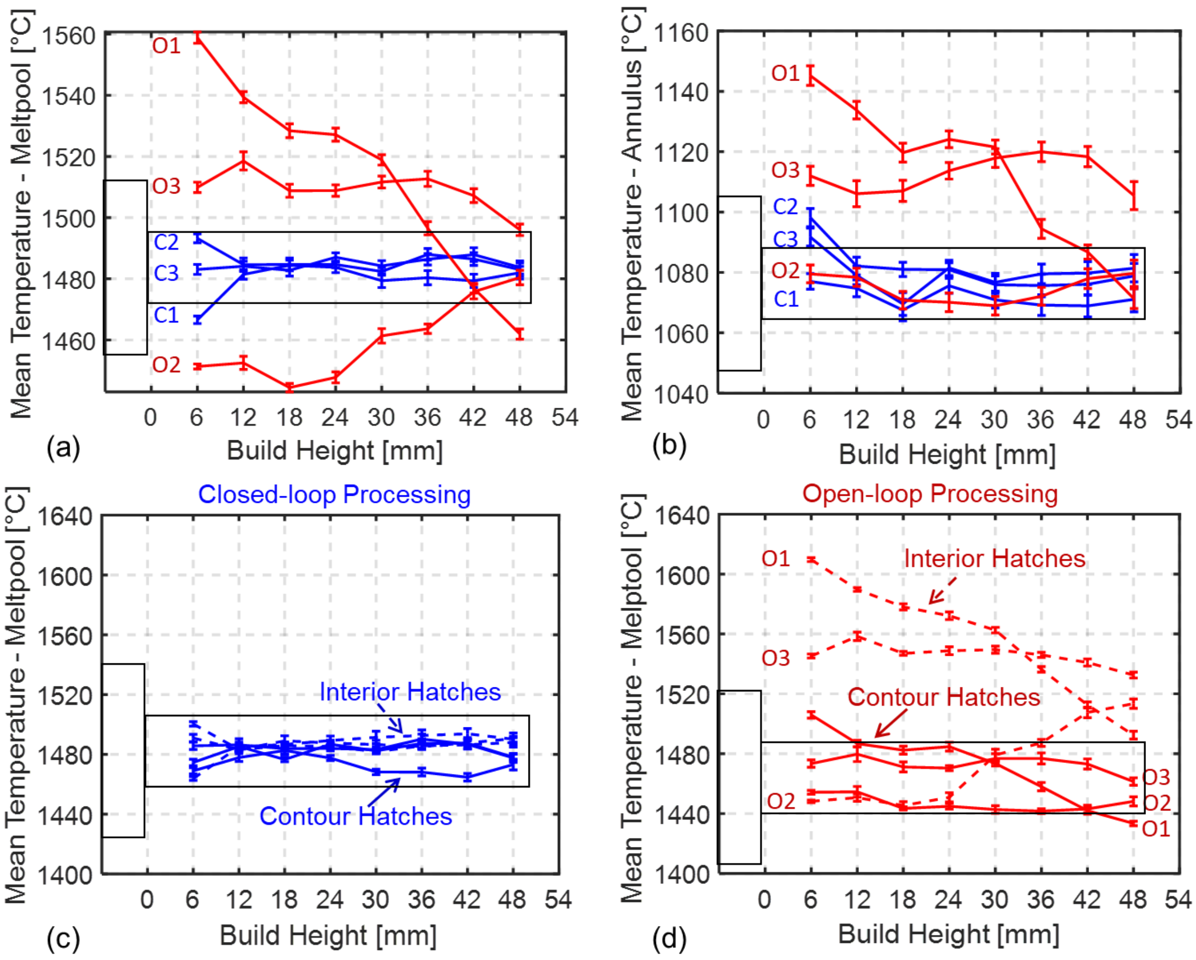

Figure 12: (a) and (b) Comparison of the average meltpool and annulus temperatures, respectively, for the open-loop processed parts (red) and closed-loop processed parts (blue). (c) and (d) Comparison of the average temperature between contour and interior hatches for closed-loop and open-loop processed parts, respectively. Closed-loop processed parts show minimal variation in the temperature of the meltpool region between the contour and interior hatches, compared to a large variation for that of the open-loop processed parts. Error bars show the mean ± 1 standard error.

As evident from Figure 13, the large variation in meltpool temperature-related characteristics for open-loop processed parts also manifests in the meltpool area. Shown in Figure 13(a) and (b), are the average area of the meltpool and annulus regions, respectively. For closed-loop processed parts, the meltpool area was 1.4 mm^2 ± 0.28 mm^2 throughout the build. In case of open-loop processing the meltpool area varies considerably (1.7 mm^2 ± 0.61 mm^2). A similar trend is observed for the annulus area in Figure 13(b).

Figure 13(c) and (d) details the manner in which the area of the meltpool region changes between contour and interior hatches. As evident from Figure 13(d) the area of the meltpool region is considerably larger for the interior hatches compared to the contour hatches within the open-loop processed parts. In case of the closed-loop processed parts, as observed in Figure 13(c), there is no prominent difference in the area of the meltpool region for the contour and interior hatches.

Depicted in Figure 14 is the variation in the size and shape of the meltpool for two representative parts (C1 and O1) at the two central sections of the build (section 4 and section 5). For the closed-loop processed part (C1), the meltpool has a relatively uniform shape and area irrespective of its location within the layer. It is observed that both the contour and interior hatches have similar meltpool characteristics. In contrast, in the open-loop processed part (O1) the meltpool area is considerably larger in the interior hatches than in the contour hatches. Figure 11 through Figure 14 illustrate the sharp contrast in the meltpool characteristics for open-loop and closed-loop processed parts. The temperature and shape of the meltpool for closed-loop processed parts are consistent (smaller variation), both within (across layers and hatches) and between different parts, compared to those from open-loop processed parts.

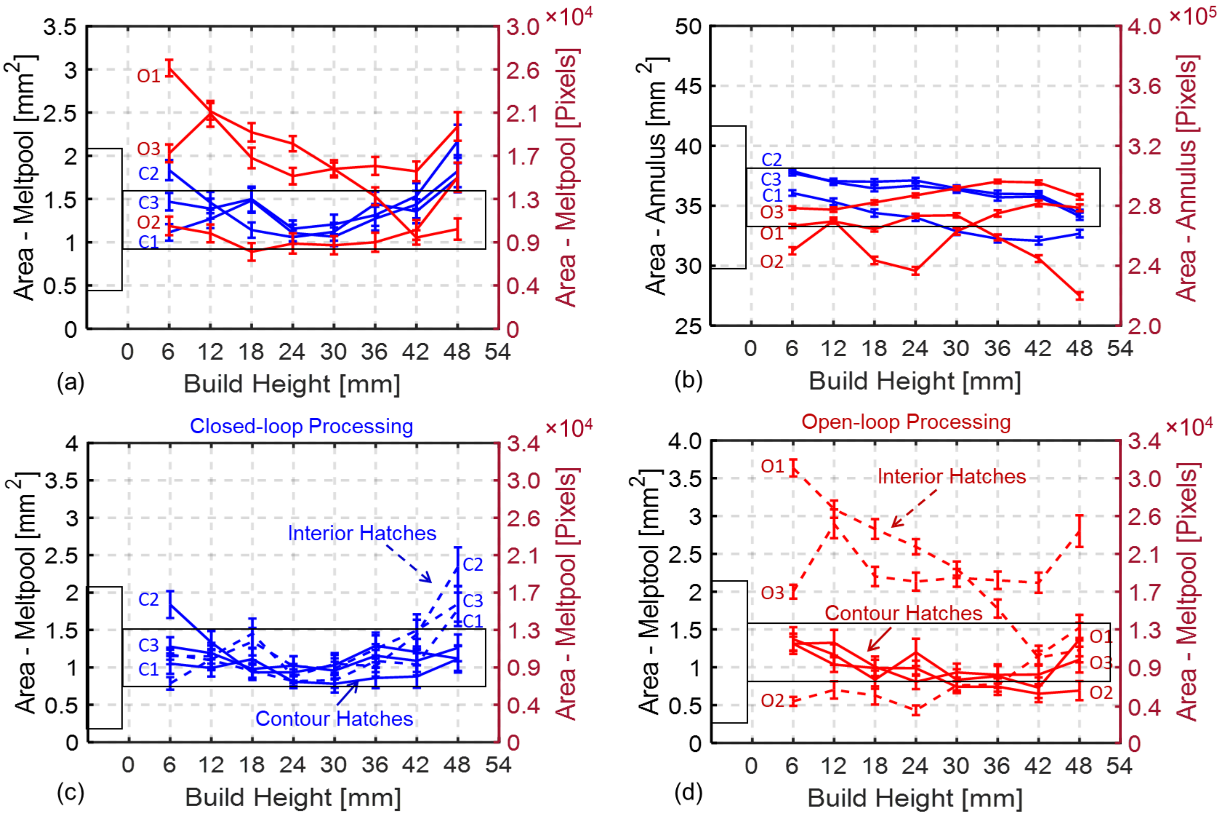

Figure 13: (a) and (b) Comparison of the area of the meltpool and annulus regions, respectively, for the open-loop processed parts (red) and closed-loop processed parts (blue). (c) and (d) comparison of the meltpool area between contour and interior hatches for the closed-loop and open-loop processed parts, respectively. Error bars show the mean ± 1 standard error.

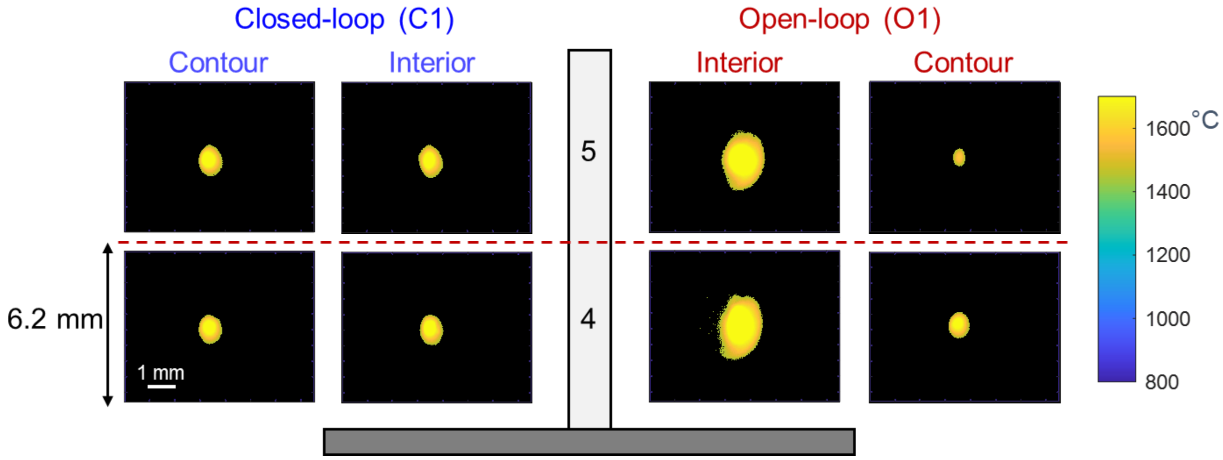

Figure 14: Visual representation of the shape of the meltpool region at the two central sections of the build, for the closed-loop and open-loop processed parts C1 and O1, respectively. The meltpool shape varies considerably for the open-loop processed part O1. Each pyrometer image is randomly selected for each section.

3.2 Effect of Closed-loop Process Control on Laser Power

Next, Figure 15 compares the laser power as a function of build height between closed-loop and open-loop processed parts. In Figure 15(a) it is observed that the overall laser power for the closed-loop processed parts increase with the build height, while the laser power for the open-loop processed parts is constant at 410 W. Furthermore, laser power in the case of closed-loop processing is higher than the laser power for open-loop processing. However, as observed from Figure 11 and Figure 12(a), the meltpool temperature for closed-loop processing is in general lower and more consistent, compared to open-loop processing.

The forgoing effect is explained in reference to Figure 15(b), where we stratified the laser power for contour and interior hatches. For closed-loop processed parts it is observed that the laser power for the contour hatches is consistently higher than the laser power for the interior hatches. This is because the contour hatches i.e., outside of the part, experience larger heat loss compared to the interior area [49].

Referring to Figure 15, there is an average difference of ~ 60 W in laser power between interior and contour hatches. A large variation (~ 50 W) between the interior and contour hatches of different builds (Figure 15 (b)) is also observed. Further, the laser power within the interior and contour hatches of the same build increases with the build height. For example, in Figure 15 (b) referring to the power variation for the interior hatches of sample C1, the controller automatically increased the laser power from 360 W to 440 W during the build.

To explain further, as the build height increases, the side-wall area is exposed to the environment and shielding argon gas from the nozzle, increasing forced convection. Therefore, to maintain the peak meltpool temperature at the setpoint of 1650°C, the controller increases the laser power for the contour of the closed-loop processed parts beyond the initially set point of 410 W for the contour hatches and decreases it below 410 W in the case of the interior hatches.

Figure 15 thus reconfirms the vital importance of modulating the laser power not only layer-by-layer as a function of build height, but also hatch-by-hatch. In other words, for controlling the meltpool temperature it is necessary to adjust the laser power in real-time, frame-by-frame and hatch-by-hatch throughout the build to maintain a set meltpool temperature, as opposed to the end of the layer.

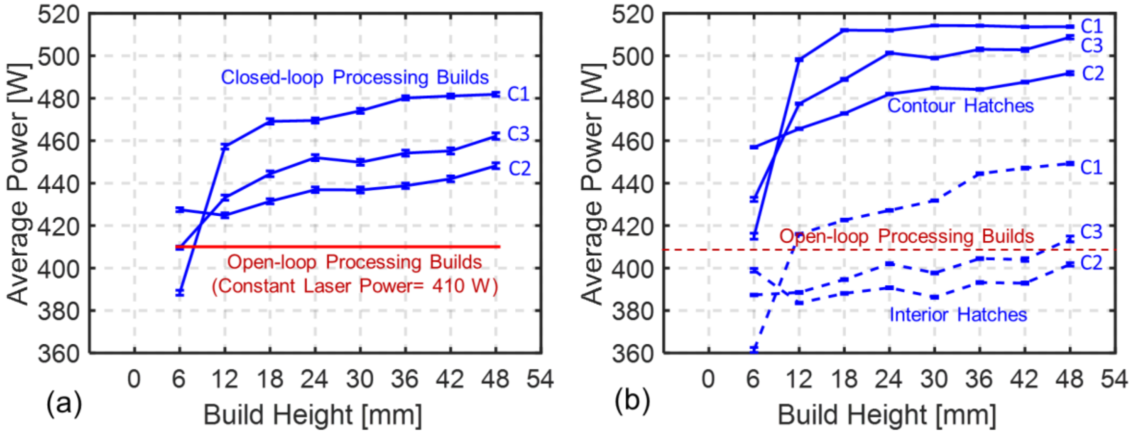

Figure 15: (a) Trend of laser power in closed-loop processing relative to open-loop processing(b) difference in the laser power between contour and interior hatches of closed-loop processing with respect to open-loop processing. Error bars show the mean ± 1 standard error.

3.3 Effect of Closed-loop Process Control on Porosity

In this section, we demonstrate that closed-loop control of the meltpool temperature mitigates variation in porosity between parts and throughout the same build. Figure 16 shows the optical micrographs for two parts from each of the open-loop and closed-loop processing conditions. Shown in Figure 16(a) are the optical micrographs for closed-loop processed parts C1 and C2. The porosity between C1 and C2 is visibly consistent in both number and size. In Figure 16(b), for open-loop processed parts O1 and O2, there is a prominent lack of consistency in number and size of pores, evident both within the same part and between parts. In both closed-loop and open-loop processing conditions, spherically-shaped pores symptomatic of gas porosity are observed. Gas porosity is likely as a result of: (a) escapement of gasses dissolved in the meltpool, and (b) release of moisture and gasses entrapped in the powder material.

Compared to C1 larger diameter pores exceeding 50 µm are observed in O1. This can be explained based on the meltpool behavior. Referring to our prior analysis of the meltpool temperature and meltpool area, in the context of Figure 12 and Figure 13 respectively, there was a larger variation in both for sample O1. Further, the relatively larger meltpool area and temperature of O1 are indicative of a high local energy density, which is liable to cause heat retention and result in vaporization of gas dissolved in the meltpool (gas porosity). The increased heat retention may also result in reheating (and possible remelting) of the previous layers, leading to a heterogenous microstructure [18, 22].

X-ray computed tomography (XCT) was performed on the T-shaped samples cut from the as-built parts (Figure 9). The samples were scanned at a voxel resolution of 10 µm, at which pores with a diameter greater than 20 µm are liable to be resolved. Accordingly, the smallest pore size considered for this analysis is 20 microns. The total percent porosity measurements from the XCT analysis using the Volume Graphics software (VGSTUDIO MAX 3.4.0) are reported in Table 3. All the closed-loop processed parts have a total volume percent porosity ranging from 0.036% to 0.043%. By contrast, for the open-loop processed parts the volume percent porosity varies from 0.032% to 0.068%. While porosity for both closed-loop and open-loop processed parts is below 0.1%, the variation in porosity volume for closed-loop processed parts is reduced compared to open-loop processed parts. The relatively large variation in the volume percent porosity of the open-loop processed part O1 is also affirmed from the XCT analysis.

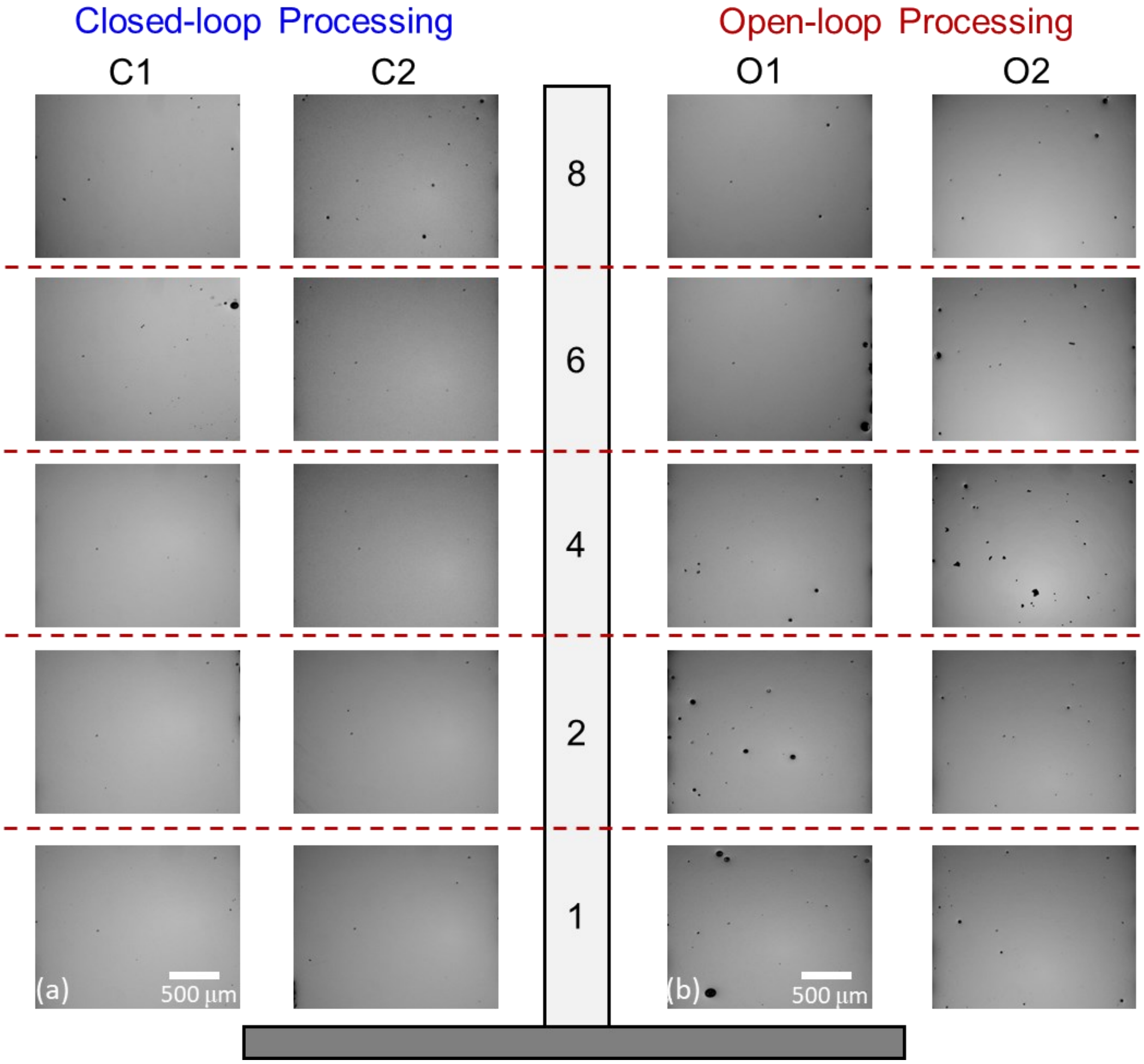

Figure 16: The optical micrography images for two closed-loop processed parts (C1 and C2) and open-loop processed parts (O1 and O2) across the 8 sub-sections. (a) The pores observed in closed-loop processed parts are consistent in size and occurrence. (b) In open-loop processed parts the number and size of the pores varies both within and between parts.

Table 3: Total overall porosity of the build for all three closed-loop and all three open-loop processed parts obtained using X-ray computed tomography (XCT). Mean and standard deviation between closed-loop and open-loop processing parts were also compared.

	Total Percent Porosity (Volume)	
Build	Closed-loop processing	Open-loop processing
1	0.043%	0.068%
2	0.036%	0.032%
3	0.039%	0.061%
Mean and standard deviation	0.039% (0.004%)	0.053% (0.019%)

Further, we stratified the volume percent porosity from XCT based on the eight sub-sections for each part. From the results shown in Figure 17, it is observed that the closed-loop processed parts have a consistent volume percent porosity throughout the build height. On contrary, the open-loop processed parts have a large variation between sections within the same part as well as across different parts.

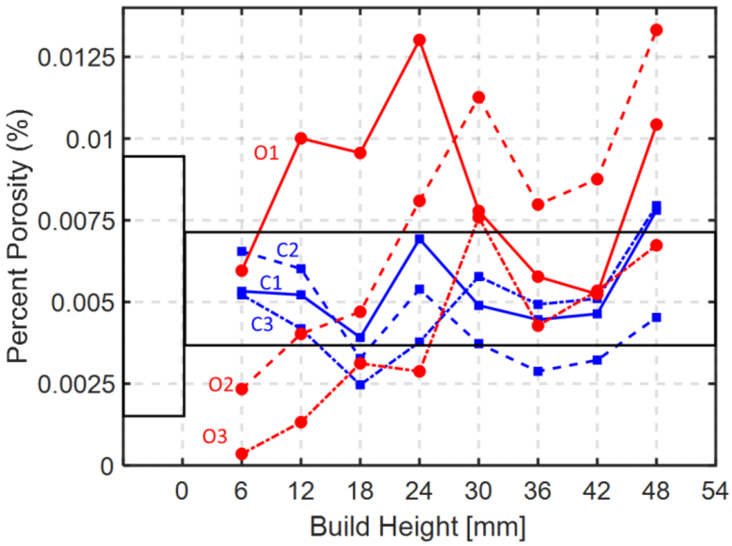

Figure 17: The volume percent porosity obtained using non-destructive X-ray computed tomography (XCT) analysis for the closed-loop and open-loop processed parts tracked as a function of the build height. The closed-loop processed parts have a consistent percentage porosity throughout the build height compared to the large variation observed in open-loop processed parts.

Next, we delineated the location of the pores by examining the occurrence of porosity between the contour hatches and interior hatches from the XCT images. As reported in Figure 18, in the case of the closed-loop processed parts, only 15% - 20% of the total number of pores occur in the interior of the build. Consequently, the vast majority of pores are located in the exterior regions (contour hatches) of the build. A similar trend is observed for the open-loop processed parts (except in the case of O1). The confinement of pores to the outer regions (contour hatches) is practically advantageous, because, these regions can be readily machined during post-processing.

As a visual comparison, Figure 19, compares a representative X-ray computed tomography slice for a layer of a closed-loop processed part C1 and an open-loop processed part O3 due to their similar level of overall porosity for sample B (~0.04%). Figure 19 confirms that there are more pores on the contour hatches of both parts. In Figure 20 the percent porosity is plotted as a function of the average temperature of the meltpool region. The porosity and meltpool temperature are tightly clustered for the closed-loop processed parts, in contrast to the large scatter observed for open-loop processed parts.

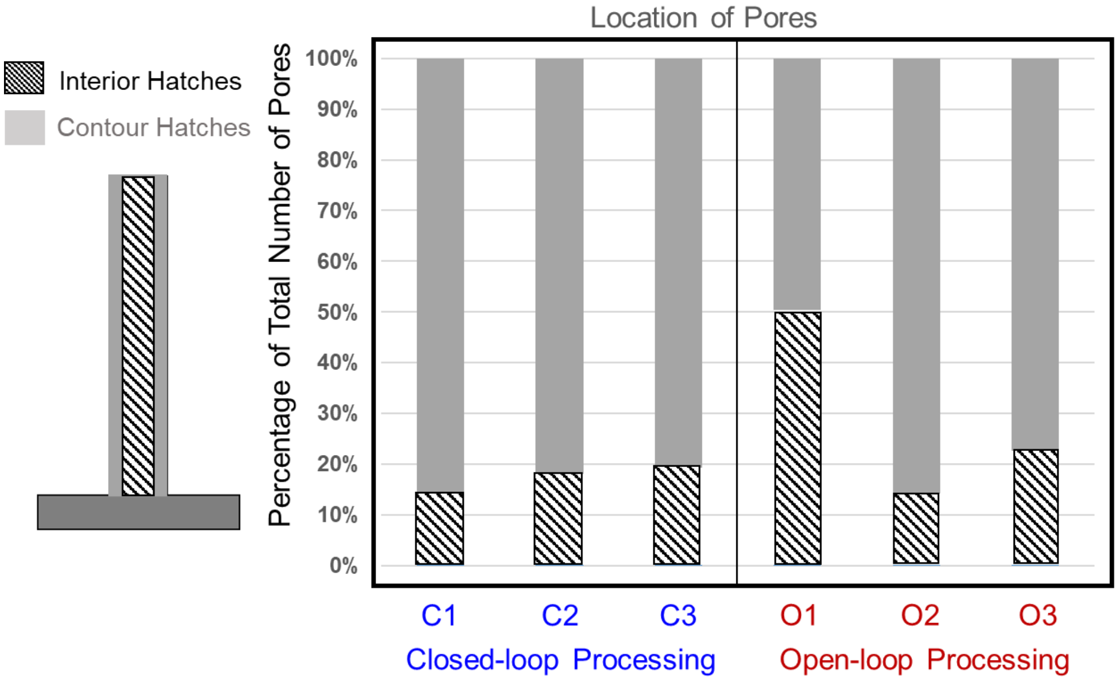

Figure 18: Stacked bar charts comparing the location of pores between the contour (gray) and interior (black & white striped) hatches. Then comparing the distribution of pores between closed-loop processed parts (left) and open-loop processed parts (right).

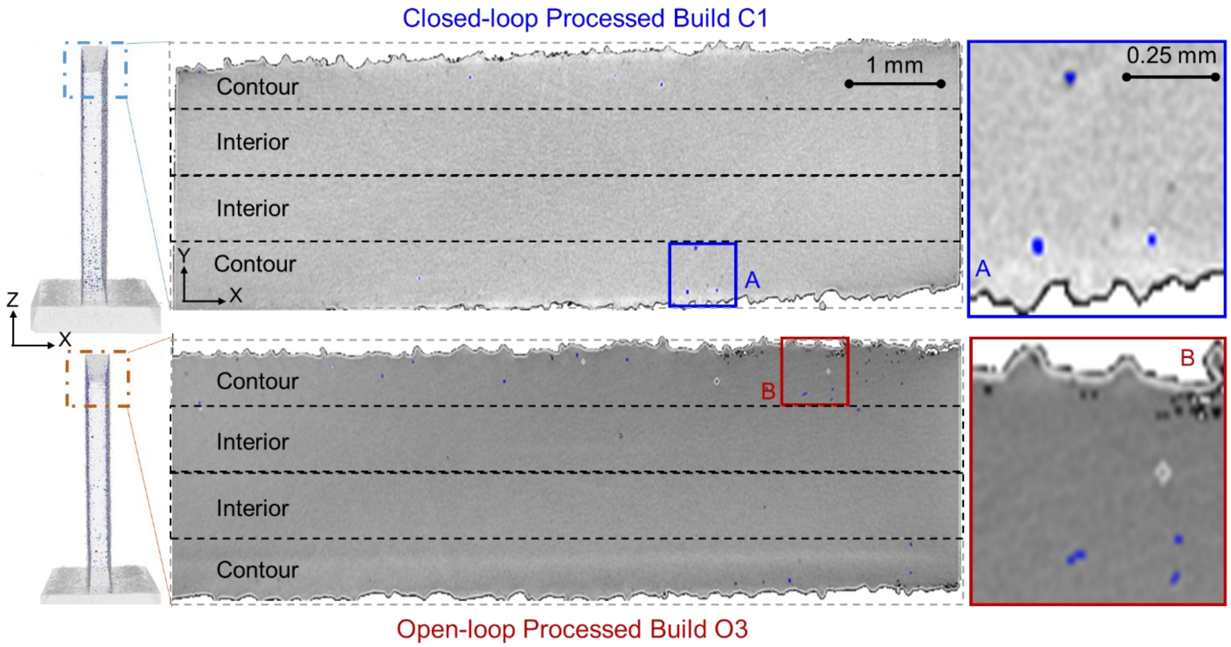

Figure 19: Visual comparison of porosity from representative XCT slices between build C1 (A) and O3 (B). Notice that there are more pores on the contour hatches relative to the interior hatches for both closed-loop and open-loop processed parts.

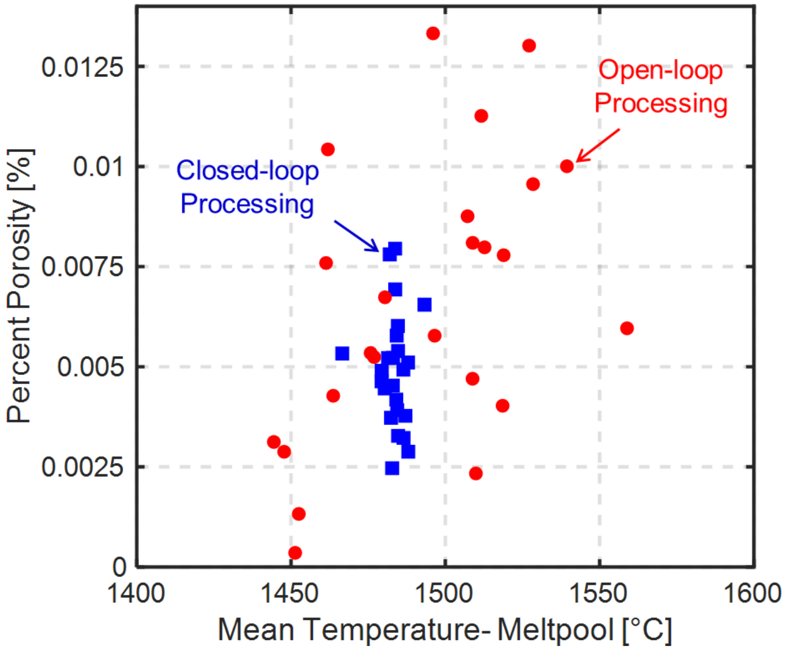

Figure 20: Scatter plot comparing the mean temperature of the meltpool region to the percent porosity in all eight sections of Sample A and B. Both closed-loop and open-loop processed parts are plotted to give a full comparison. All three closed-loop processed parts stay clustered due to the constancy between and within parts. open-loop processed parts are scattered due to minimal constancy between parts.

3.4 Effect of Closed-loop Process Control on Microstructure

3.4.1 Morphology

Figure 21 shows SEM images of the microstructure in different areas along the SS 316L parts for closed-loop and open-loop DED processing conditions. These areas are indicated on the corresponding schematic adjoining the SEM images by letters L, M and R to represent the left, middle and right areas of the cross section, respectively. The observations are as follows.

The microstructure in the areas closer to the free sidewall surfaces marked as zones L and R is composed entirely of columnar dendrites for parts produced under both open-loop and closed-loop processing conditions. However, there is a significant difference in the morphology of the microstructure in the middle area (M) between the open-loop and closed-loop processing methods.

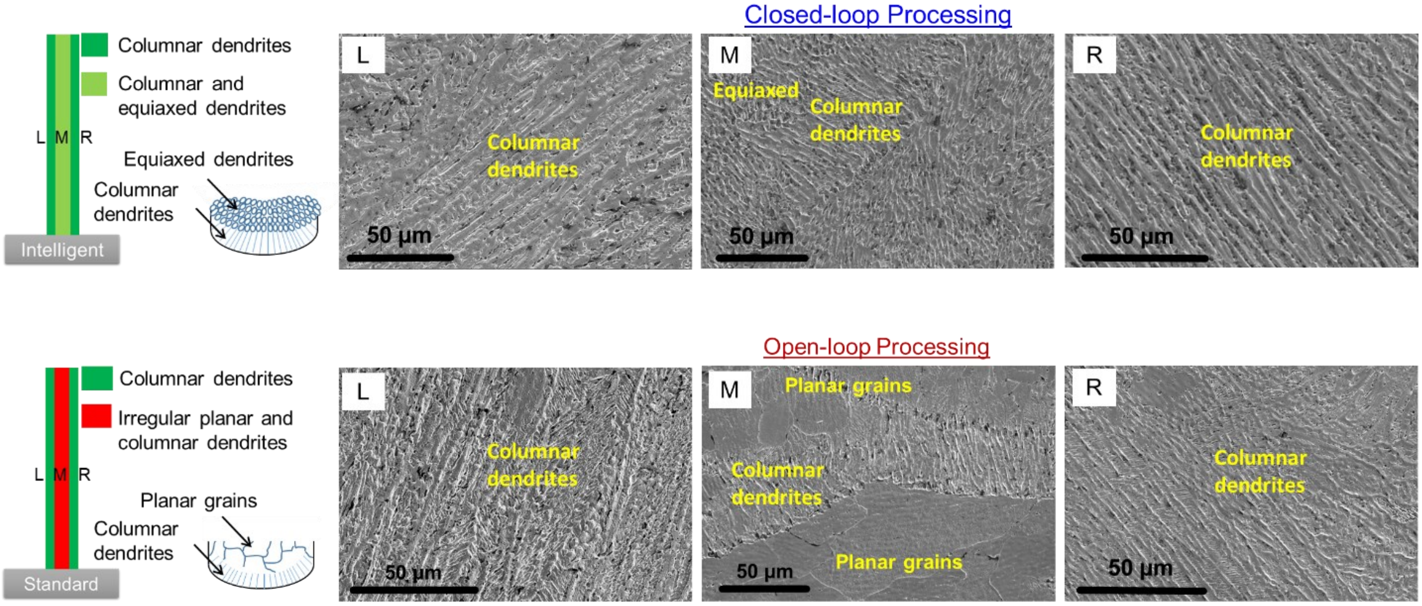

Figure 21: SEM images of the microstructure in different regions of the SS 316L parts as indicated in the representative schematics of the cross-sectional view shown on the left. Top row shows the microstructure observed for the closed-loop processed part C1 and bottom row shows microstructure for open-loop processed part O3. The closed-loop processed parts form dendritic microstructures throughout the build. The contour hatches result in columnar dendritic microstructure, while the interior hatches result in both columnar and equiaxed dendrites. In contrast, the open-loop processed parts show columnar dendritic microstructure on the contour hatches, while the interior resulted in a mix of irregular planar grains and columnar dendrites.

The microstructure of a closed-loop processed part in the area M (Figure 21, top row) is dendritic with columnar dendrites at the periphery of the deposition tracks and equiaxed dendrites towards the center of the tracks. This type of dendritic microstructure is typical for DED-processed parts as observed by Farshidianfar *et al.* [29, 43] and Akbari *et al.* [28, 50]. In sharp contrast, for parts produced under open-loop processing conditions (laser power fixed at 410 W, Figure 21, bottom row), the microstructure at the center (M) is composed of irregularly shaped, planar grains that resemble those of a cast alloy. The transition of the dendritic grains into block-shaped, irregular planar grains is evident from the fainter dendritic cells observed within the boundaries of some planar grains prior the complete transition. The transformation of the dendritic microstructure into planar grains stems from the accumulation of heat and overheating of interior tracks as the build process continues layer-upon-layer.

In closed-loop processing, the feedback control of the meltpool temperature to 1650°C regulates the deposition power to maintain a constant temperature along the build, as well as between the contour and interior hatches, as evident in Figure 12, Figure 13, and Figure 14. When the laser power is fixed, as in the open-loop processing, the temperature increases as a function of the build height due to the tapered cross-section of the part. The temperatures reached in the previously deposited material can surpass the melting point, which in turn, promotes the re-solidification of the grains in previous layers, leading to the formation of coarse microstructure.

To further investigate this phenomenon, the microstructures from closed-loop and open-loop processing are compared for different heights along the build in Figure 22, which shows the difference in microstructure between closed-loop and open-loop processing at four different sub-sections along the build direction (each sub-section was 6.2 mm tall). It is observed that the microstructure formed during closed-loop processing is consistently of dendritic type throughout the build. In the case of the parts processed under open-loop conditions, the heterogeneity in microstructure is evident from the alternating dendritic and planar morphologies. Yang *et. al.* [51] reported a similar heterogenous microstructure in DED of SS 316.

In welding, which is analogous to DED, substantial grain coarsening has been observed in previously deposited material [20, 52]. The underlying material adjacent to the weld track is subjected to a range of temperature that may exceed the melting point, resulting in grain coarsening. Previous research has showed that the deposition process in DED induces thermal cycling, with temperature excursions sufficient to cause re-solidification of previously deposited tracks [53]. This phenomenon extends from the melt periphery and depends predominantly on the high temperature gradient (G) to growth rate (R) ratio [54], which is explained in depth in the forthcoming Sec. 3.4.2.

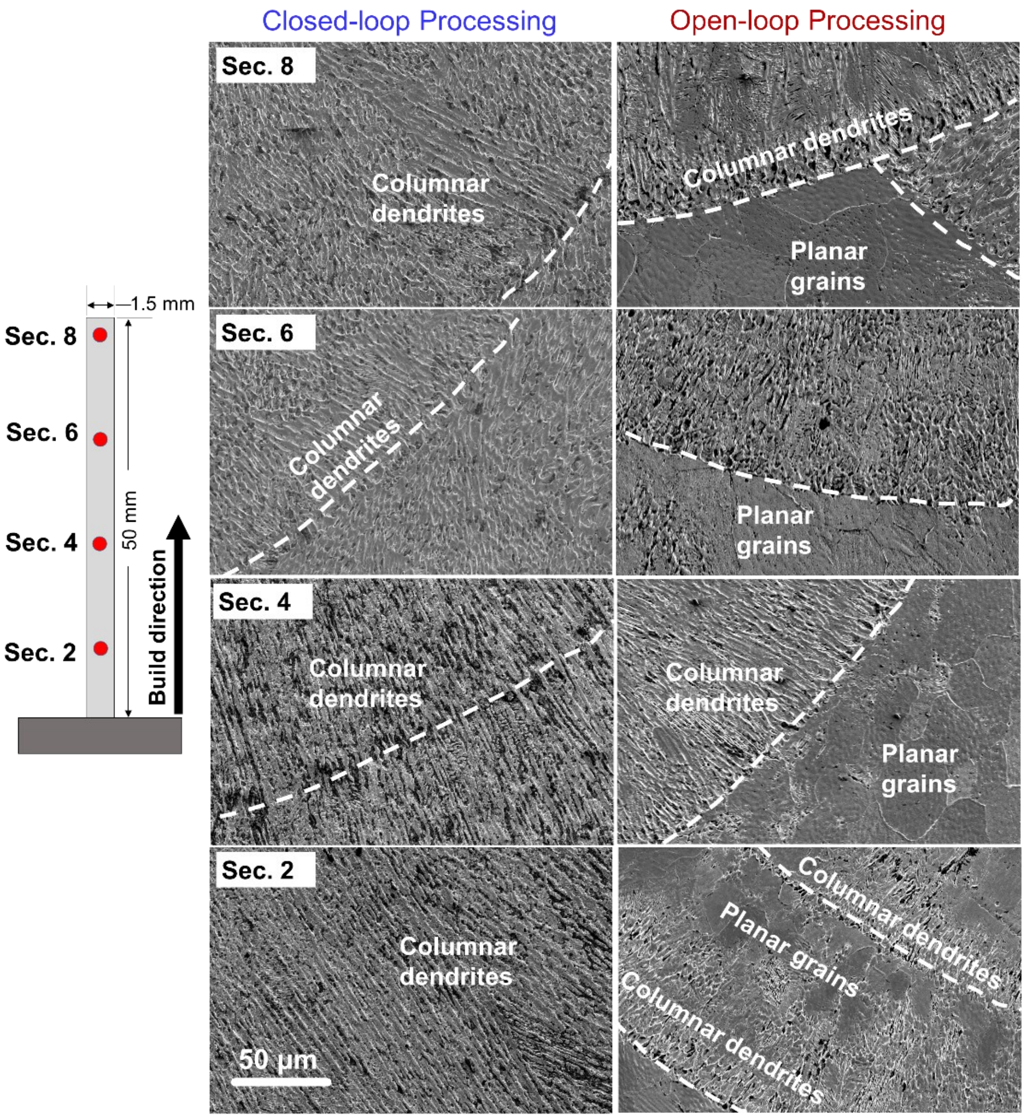

Figure 22: The SEM images of the microstructure at different sections along the build direction. The SEM images on the left column represents the microstructure from closed-loop processing (C1) and the right column represents the microstructure from open-loop processing (O1). Each sub-section is ~6.2 mm tall and is indicated by red dots on the t-shape legend on the left. Dotted curves indicate meltpool boundaries.

3.4.2 Correlation of microstructure with cooling rate and thermal gradients

The aim of this section is to explain the thermal phenomena that lead to the microstructure morphology observed in Figure 22. Specifically, we show that the closed-loop control of the meltpool temperature mitigates inordinate increases in the build temperature and thus alleviates re-solidification of the dendrites in closed-loop processed parts. On the contrary, for open-loop processed parts the unmitigated increase in temperature causes the dendrites to re-solidify into coarse planar-shaped grains.

The key idea is to estimate the cooling rate from the microstructure using an empirical relationship obtained from the literature [55]. The approach is as follows. First, we measured the primary dendritic arm spacing (λ_1) from the SEM micrographs of the microstructure for both closed-loop and open-loop processed parts. Next, the cooling rate is estimated using the empirical relationship proposed by Katayama and Matsunawa [55] for stainless steels. This empirical relationship connecting the grain size and cooling rate is as follows,

$$\lambda_1 = 80(\varepsilon^{-0.33}) \tag{1}$$

In Eqn. (1)), λ_1 is the primary dendrite spacing in micrometers [µm], and ε is the cooling rate in Kelvin per second [$\mathrm{K \cdot s^{-1}}$]. This relationship was also used by Elmer *et. al* [54] and Galicki *et. al.* [56] for cooling-rate calculations of different stainless steel alloys*,* and by Akbari and Kovacevic in DED of SS 316L [28]. Since the region near the outside surfaces has a columnar microstructure for both types of parts, it allows the measurement of primary dendrite arm spacings (PDAS, λ_1). Figure 23 (a) is a representative SEM image of the columnar microstructure, which was used for PDAS calculations.

The mean and standard deviation of PDAS along a distance of 250 µm were calculated from two separate SEM images at each of the 8 equidistant 6 mm sub-sections along the build direction (the regions where the SEM images were taken are shown in Figure 10). Regions of the SEM with resolidified coarse grains and poorly defined dendritic structures were not used in the analysis. Figure 23(b) shows the mean primary dendritic arm spacing (λ_1) measurements along with the ± 1σ error bars for the open-loop (O1) and closed-loop (C1) processed parts.

The dendrite arm spacing increases with the build height for both closed-loop and open-loop processed parts. The increase in the dendritic arm spacing, and thus coarsening of the microstructure, as the build height increases is symptomatic of heat retention. The increase in meltpool area towards the end of the build observed in Figure 13(a) is indicative of heat retention for both open-loop and closed-loop processed parts. Heat retention increases with distance from the build plate because the heat sink effect of the build plate reduces, and the laser path becomes shorter due to the progressive tapering of the part length. The coarsening of the grain size with build height is consistent with Akbari *et al.* [28].

Figure 24 depicts the change in cooling rate calculated from the relationship in Eqn. (1)), i.e., $\lambda_1 = 80(\varepsilon)^{-0.33}$ as a function of build height. The steep reduction in cooling rate as the distance from the build plate increases is an indicative of heat retention (slower heat dissipation). A similar trend is observed for both open-loop and closed-loop processed parts.

Next, the cooling rates (ε), estimated from the dendrite arm spacing (λ_1), from Eqn. (1)) are used to calculate the solidification velocity, R [$\mathrm{m \cdot s^{-1}}$], via the following relationship [56],

$$R = \frac{\varepsilon}{G} \tag{2}$$

where G is the temperature gradient [$\mathrm{K \cdot m^{-1}}$] within the meltpool [56]. Thus, using the cooling rate (ε) from Eqn. (1)) and temperature gradients (G), a range of solidification velocities (R) can be calculated. The temperature gradient is mainly dependent on the volume of the molten material, and the solidus and boiling temperatures of the alloy [56].

Figure 25 shows calculation procedures for the thermal gradients (G) and solidification front velocities (R). If the solidification starts from the periphery of the deposition track towards the heat source as shown in the optical and SEM images of the cross section (Figure 25 (a) and (b)), the liquid region could take any value between the solidus temperature of SS 316L (~1371°C) and the maximum meltpool temperature, which could reach up to the boiling point (2726°C) [56].

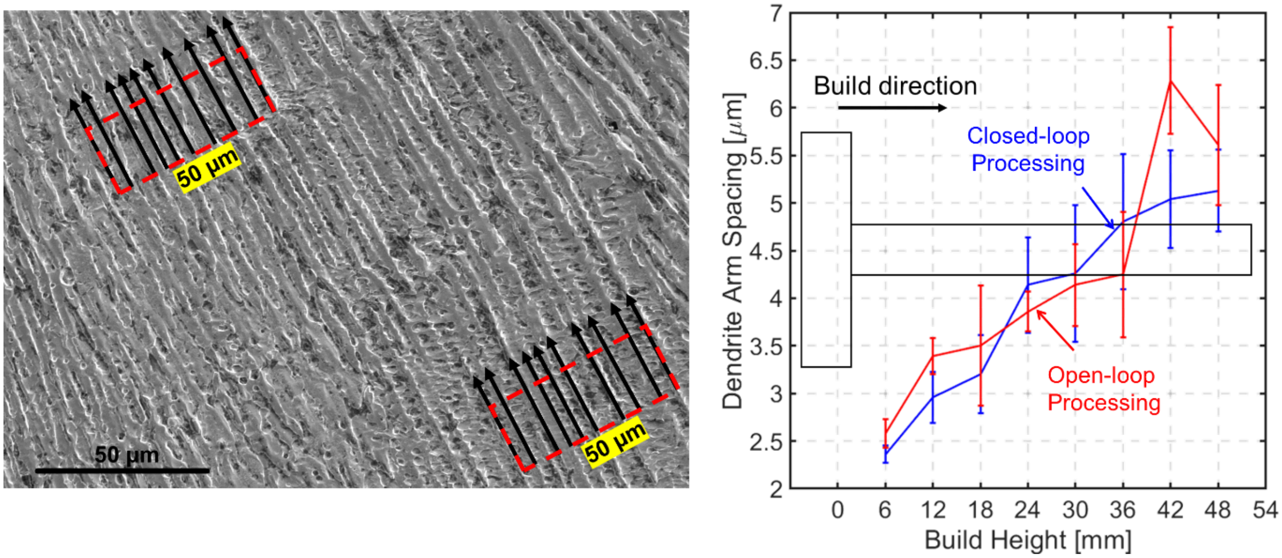

Figure 23: (a)Measurements of primary dendrite arm spacing (PDAS) for a representative SS 316L build C1. A representative SEM image of the dendritic microstructure from which PDAS were measured; (b) Primary dendrite arm spacings as a function of build height for representative parts O1 and C1. Error bars show the mean ± 1 standard error.

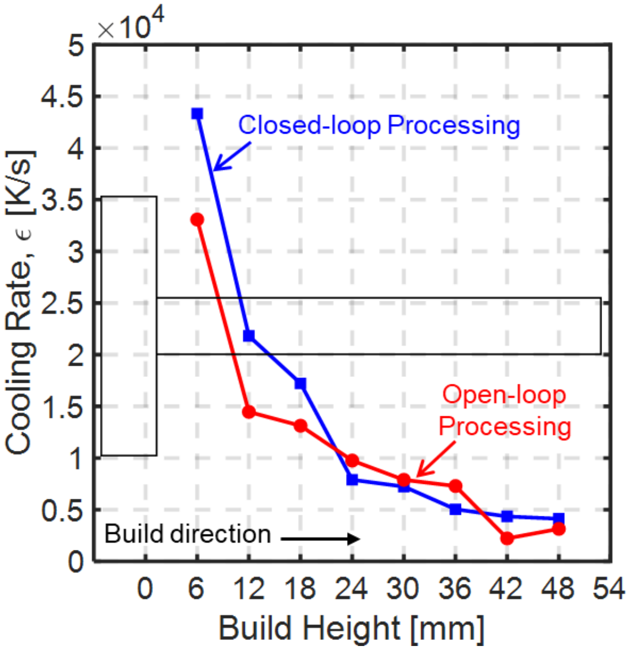

Figure 24: The mean cooling rate, ε, measured from the primary dendrite arm spacing at 8 different sections along the build. The data is representative of parts O1 and C1.

Accordingly, a range of thermal gradients can be calculated by taking the difference between solidus temperature (T_s = 1371°C) and meltpool temperature (T_m) over the distance (d) between the meltpool periphery and the heat source. In this work, the distance (d) is the radius of the meltpool track, r_m, for the entirety of the temperature range, assuming $\theta = 0°$. This produces the minimum distance (d) that generates the maximum thermal gradient as indicated in Figure 25(c).

$$G = \frac{T_m - T_s}{r_m} \tag{3}$$

Here, we assume that the solid-liquid interface maintains a spherical shape even as it moves continually with the center of the laser path [57]. In this work, the radius of the meltpool (r_m) is estimated from optical images of the cross-section normal to the laser path. Seventy optical images for each type of processing condition were analyzed along the build height. For the closed-loop processed parts, the average meltpool radius (r_m) was 311 µm with standard deviation 34 µm. In the open-loop processed parts, the average meltpool radius (r_m) was 329 µm with standard deviation of 45 µm. Based on these extensive measurements of the average meltpool radius, we fixed r_m=300 µm as a good estimate of the minimum radius that results in the maximum thermal gradients along the build direction. Using a fixed meltpool radius also simplifies the calculations of the temperature gradients (G) in Eqn. (3). The temperature gradient becomes only a function of difference between meltpool temperature (T_m) and the constant solidus temperature (T_s = 1371°C, melting point of stainless steel 316L). We implicitly assume that the temperature gradient remains constant in different parts of the meltpool based on an earlier assumption that the solid-liquid interface maintains a spherical shape with the laser path throughout the process.

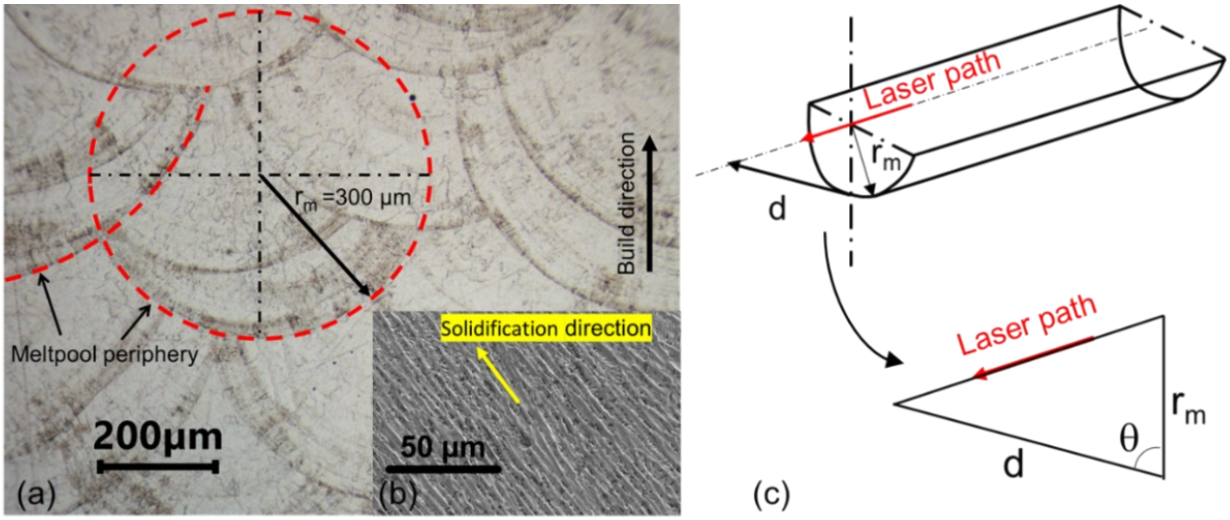

Figure 25: Calculation procedures for thermal gradients, G, and solidification front velocity, R, (a) An optical micrograph of the cross sectional view of a representative build that is normal to the direction of the scan (laser is moving in and out of the plane of the page), (b) an SEM image of the solidification direction of the dendritic structure, which initiates from the periphery of the meltpool towards its center, and (c) schematic representation of a single track that is used to illustrate calculations of thermal gradient.

The thermal gradient (G) vs. solidification velocity (R), obtained from Eqn. (2) and (3), is plotted in Figure 26(a) on a logarithmic scale for each of the eight sub-sections of a build. In Figure 26(a), even though there was a continuum of G vs R across the build height, for the sake of explanation we discretized the G vs. R at discrete points. Since the meltpool temperature of the open-loop processed parts varies considerably (Figure 12, Sec. 3.1), the thermal gradient has a large range.

On the other hand, the closed-loop processed parts have a narrow window for the thermal gradients as the peak meltpool temperature was controlled at 1650°C. Accordingly, the thermal gradient G corresponding to the closed-loop processed parts is between 0.9×10^6 and 1×10^6 $K \cdot m^{-1}$, as indicated by the smaller (blue) box on Figure 26(a). In contrast, for the open-loop processed parts, the thermal gradient can take any value from 1×10^5 $K \cdot m^{-1}$ to 45×10^6 $K \cdot m^{-1}$, a range that is bounded by the larger (red) box on the same graph. In other words, n closed-loop processed parts (closed-loop processing), the G vs R is constrained in a narrow window compared to open-loop processed parts (open-loop processing).

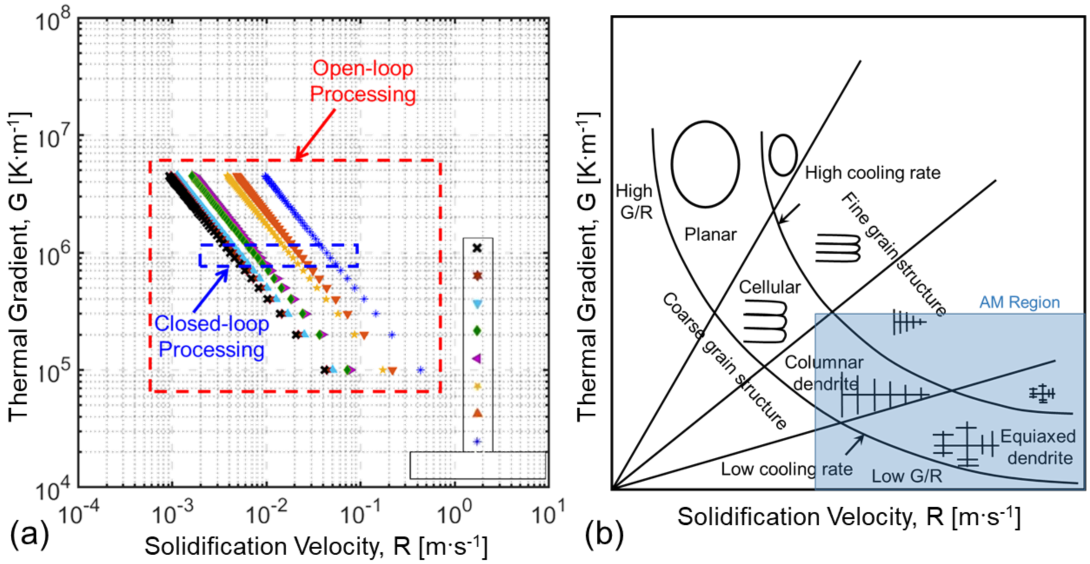

Figure 26: (a) Plot of temperature gradient (G) and solidification velocity (R) estimated from the microstructural features using equations (2) and (3). The symbols represent G and R estimates from different locations within the build, shown in the inset schematic of the build cross section. The red box contains all possible G and R conditions for open-loop processing, while the blue box contains conditions for the closed-loop processing. The closed-loop processing provides a much smaller processing window, resulting in a more homogeneous microstructure. (b) Schematic representation of the effect of thermal gradient G and the solidification velocity R on solidification microstructure [58].

Figure 26(b) shows a schematic representation of the effect of thermal gradient and solidification velocity on the microstructure. An important factor in determining the morphology of the microstructure evolved is the ratio of temperature gradient and solidification velocity at the solid-liquid interface, termed the G/R ratio [59]. Based on the value of ratio G/R as indicated on Figure 26(b), the solidification structure can be equiaxed dendritic, columnar dendritic, cellular, or planar.

The maximum possible value of G/R ratio calculated for open-loop processing in this work was 4.9×10^3 K·s·mm^{-2}. This G/R ratio is less than 7×10^3 K·s·mm^{-2}, which is the minimum theoretical value of G/R that typically results in planar grains [60]. Accordingly, a solidification front for planar grains becomes unstable and the solidification proceeds with a cellular or columnar dendritic structure [61]. Hence it is deduced that the planar-like morphology observed in the case of open-loop processing, observed in Figure 21 and Figure 22, resulted from heat accumulation during deposition of subsequent layers and not during the actual deposition of a layer.

Since, the cooling rate decreases with the build height, heat accumulates near the top. Therefore, in the case of open-loop processed parts, the layer directly below the deposited layer is exposed to a high temperature, sufficient to cause re-solidification of the dendritic microstructure and their subsequent transformation into a coarse-grained structure. Consequently, the type of microstructure evolved for the open-loop processed parts is heterogenous in nature; it consists of both columnar dendritic grains and planar type grains. Controlling the meltpool temperature with closed-loop processing reduces the high thermal gradients and inhibits the re-solidification of previously deposited layers. As a result, the microstructure for closed-loop processed parts is homogenous, and consists of dendritic structure as shown in Figure 21 and Figure 22.

3.4.3 Material Phase Identification and Elemental Composition

Figure 27 shows the XRD results from two different SS 316L parts, C3 and O2, representing closed-loop and open-loop processing methods, respectively. From Figure 27 it can be deduced that the microstructure of parts from both closed-loop and open-loop processing methods consists of a single phase (γ-Fe), consistent with what is expected for SS 316L, without any detectable presence of other phases. However, this does not preclude the possibility of minor phases in the microstructure, which are beyond the detection capability of XRD. Although the columnar dendritic structures usually grow in a specific orientation, no evidence of preferred crystallographic orientation was observed by XRD for any of the processing methods, as the intensities follow expected trends. Similar XRD results in the DED processing of SS 316 have been reported by other researchers [62-67].

In general, the primary solidification phase depends on two factors – the cooling rate and the alloy composition. High cooling rates promote the solidification of stainless steels in only a single-phase, depending on the weight concentration of Cr and Ni in the alloy [54, 68]. A single phase austenitic stainless steel is obtained at high cooling rates when the Cr:Ni concentration ratio (by weight) is less than 1.51, i.e., the concentrations of Cr and Ni are comparable in the alloy. This is because the high cooling rate reduces the diffusivity of solute atoms and thus segregation, which consequently, precludes additional phase formation [54, 62].

Figure 28(a) and (b) show the change in the elemental composition of as-built SS 316L parts using closed-loop and open-loop processing methods, respectively. It is observed that the concentrations of the three main elements (Fe, Cr, and Ni) remain uniform within the parts. Moreover, their corresponding levels are also consistent between parts. In other words, there is no significant variation in composition within a part across layers, nor is there a difference in the composition of the microstructure resulting from the closed-loop and open-loop processed methods. Note that this does not preclude micro-segregation.

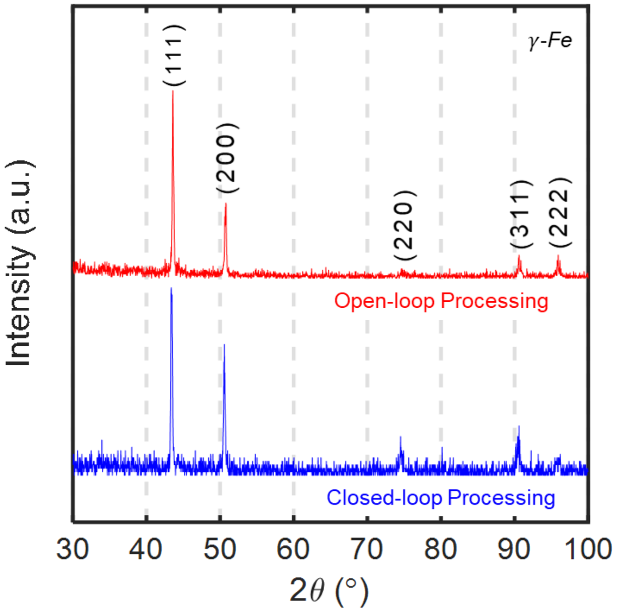

Figure 27: X-ray Diffraction patterns of as-built SS 316L parts using closed-loop (blue) and open-loop (red) processing methods. The two types of parts have a single phase (γ-Fe). There is no difference in the microstructure phases between closed-loop and open-loop processing.

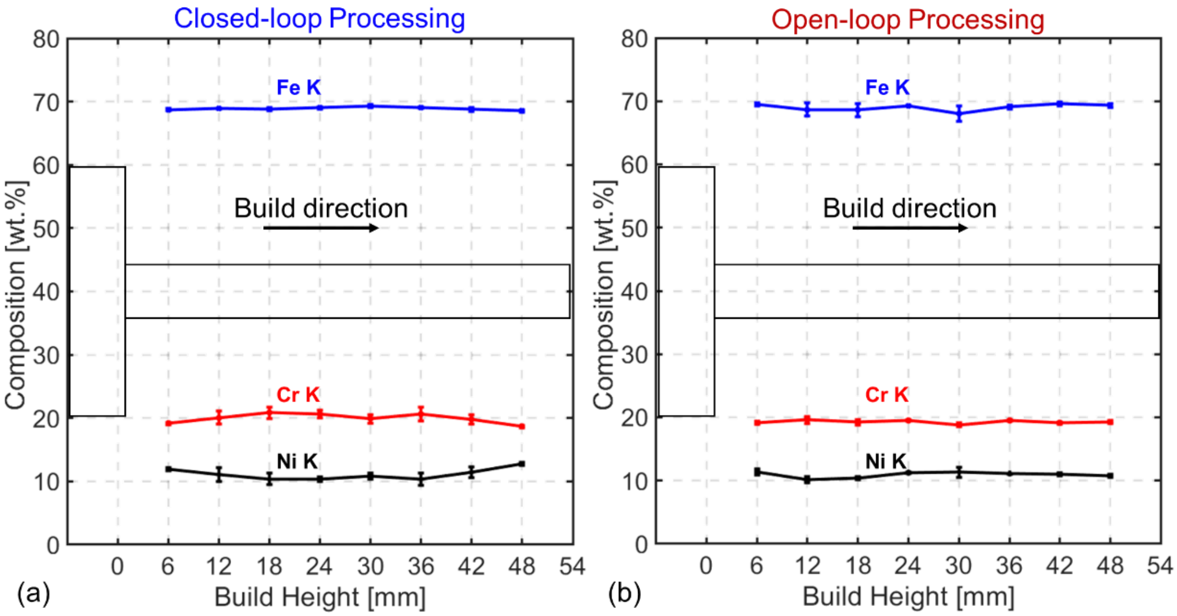

Figure 28: EDS point analysis of as-built SS 316L parts. There is no discernable change in the elemental composition (wt.%) within and between parts deposited using either (a) Closed-loop processing, and (b) open-loop processing as a function of build height. Error bars show the mean ± 1 standard error.

As discussed in Sec. 3.4.1, there is a significant difference in the microstructure morphology between closed-loop and open-loop processed parts. Referring to the previous SEM images shown in Figure 21 and Figure 22, the closed-loop processed parts have a dendritic microstructure with both columnar and equiaxed dendrites. The open-loop processed parts, on the contrary, contain columnar dendrites on the contour, and non-uniform planar grains towards the center of the part. Hence it is important to investigate the degree of micro-segregation, as well as demarcate elemental variation between different microstructural morphologies.

To assess the elemental variation, EDS line scans were performed on two representative parts, as exemplified in Figure 29. From Figure 29(a), in the context of the closed-loop processed part, it is observed that there is a small yet discernable variation in the composition of Cr and Ni across the columnar dendrites. An increase in the Cr content correlates with a decrease in the Ni content. This variation in Cr and Ni is typically associated with the formation of a second BCC ferrite phase (δ-Fe) on the sub-grain boundaries [69-71]. However, the amount of this second ferrite phase is far too small to be detected using XRD analysis as shown in Figure 27.

On the other hand, the results of EDS line scan performed on an open-loop processed part (Figure 29 (b)) shows a uniform elemental composition across the planar grains. The result of EDS line scan analysis performed on different morphologies agrees well with those obtained from EDS point analysis conducted at different sections of the parts. In other words, EDS analysis affirm that the composition is homogenous within the parts and there is no significant difference in elemental composition between parts processed using closed-loop and open-loop processing methods. This is an important observation as it shows that the closed-loop processing of parts produced with controlled meltpool temperature does not lead to potentially deleterious changes in chemical distributions.

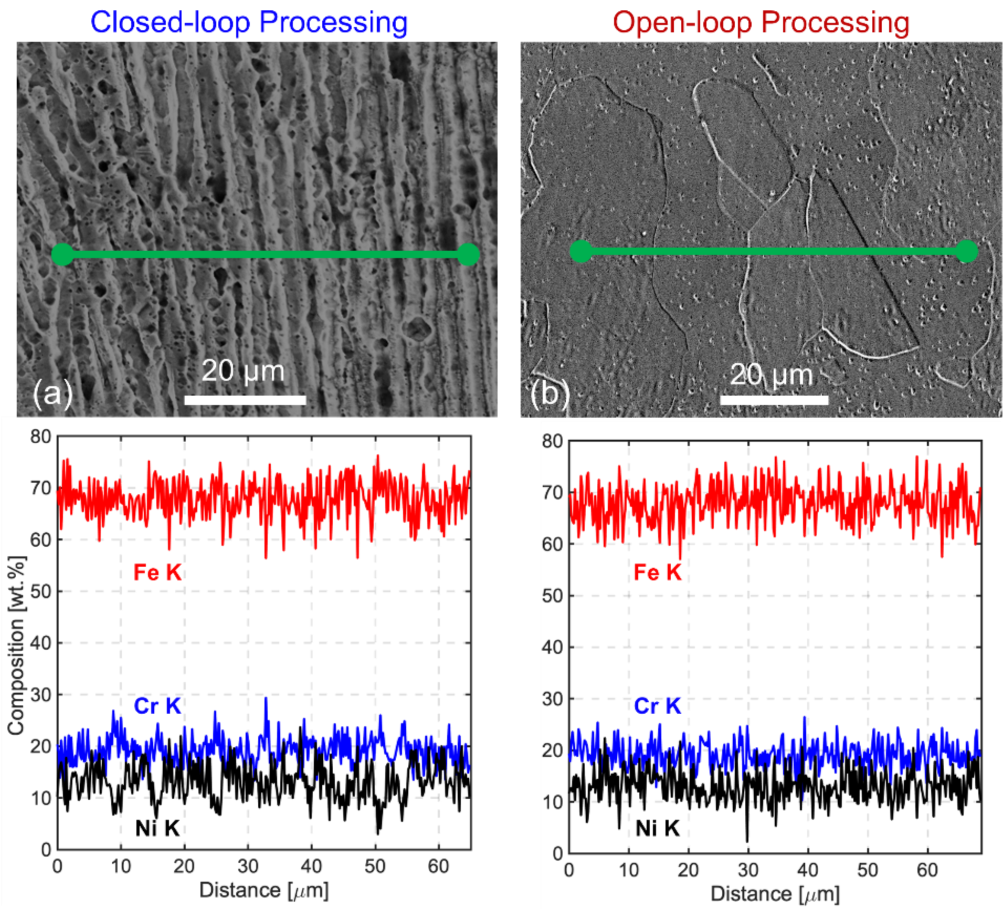

Figure 29: EDS line scan analysis of different microstructures from (a) Closed-loop processing and (b) open-loop processing. The elemental composition is uniform within the parts and there is no variation in elemental composition between the two processing methods, albeit the microstructure evolved is different. EDS data were collected from samples O1 and C3.

3.4.4 Microhardness

Figure 30 reports the microhardness measurements for both closed-loop and open-loop processed parts as a function of the build height. Control measurements are also reported for the build plate and interface region (demarcated as I on the X-axis). From the microhardness profiles, it is observed that for a particular build height the overall mean level of the microhardness measurements from the closed-loop processing ($HV_{0.5}$= 174, Figure 30(a)) does not differ significantly from that of the open-loop processing ($HV_{0.5}$ = 172, Figure 30(b)). However, there is a significant difference in the standard deviation between the closed-loop and open-loop processing. The overall standard deviation of microhardness (σ) from open-loop processing is ~85 $HV_{0.5}$, which is significantly larger than that of closed-loop processing, σ ~ 60 $HV_{0.5}$. The microhardness readings are reported in the Appendix.

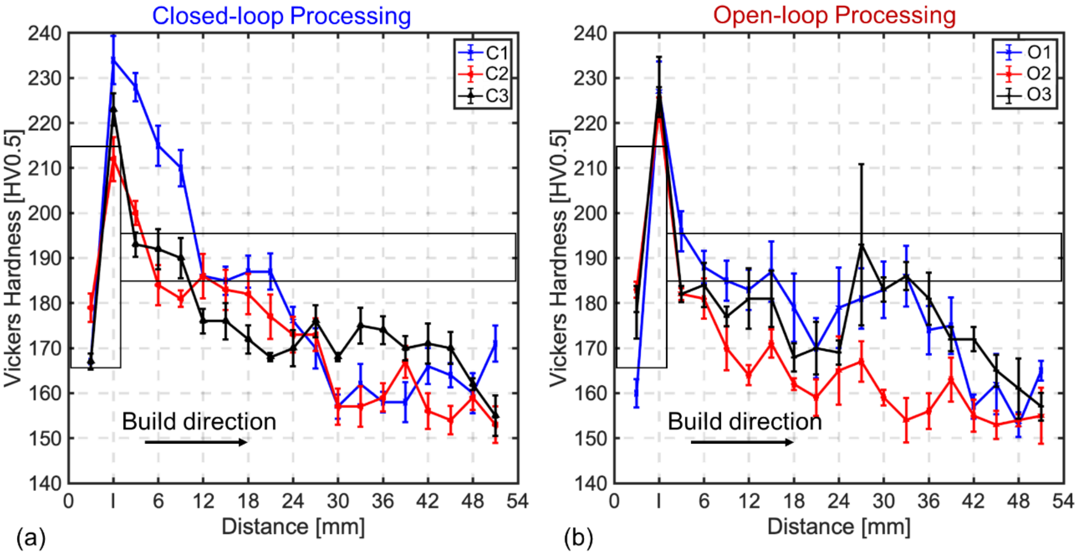

Figure 30: Microhardness profiles along the height of different SS 316L parts using (a) Closed-loop processing and (b) open-loop processing. Five hardness readings were taken at every 3 mm along the height of the build (10 readings per interval). The error bars are ± 1 standard deviation long. The microhardness for both the open-loop and closed-loop processed parts decreases with the build height due to increase in the grain size (λ_1). However, for open-loop processed parts the variation in microhardness, both between and within the same build, is large due to heterogeneity in the microstructure. Error bars show the mean ± 1 standard error.

This larger variation in microhardness in open-loop processed parts is a result of the heterogeneity in the microstructure. This phenomenon was further investigated by making several microhardness indents on the planar and dendritic morphologies observed in an open-loop processed part and compared along the cross section of the build at the same height (sub-section). Figure 31 shows the variation in microhardness marks resulting from indents on the different grain morphologies. From the results reported in Table 4, it was observed that the dendritic microstructure has a significantly higher microhardness than that of the planar morphology. The larger *average* microhardness values for the distance smaller than 12 mm in one of the closed-loop processed parts are likely to be associated with several factors such as the proximity to the build plate, which acts as a heat sink, and the inherent stochasticity of the process.

A gradual reduction in microhardness is observed in the build direction regardless of the processing method. This observation further confirms the results from the primary dendrite arm spacing (Figure 23(b)). The primary dendritic arm spacing (λ_1) increases with the build height – the microstructure becomes coarser with the build height –as the cooling rate (ε) decreases along the build. An increase in the grain size consequently results in a reduction in the microhardness for both the closed-loop and open-loop processed parts. However, the heterogeneity in microstructure for the parts produced under open-loop processing conditions magnifies the variation in microhardness.

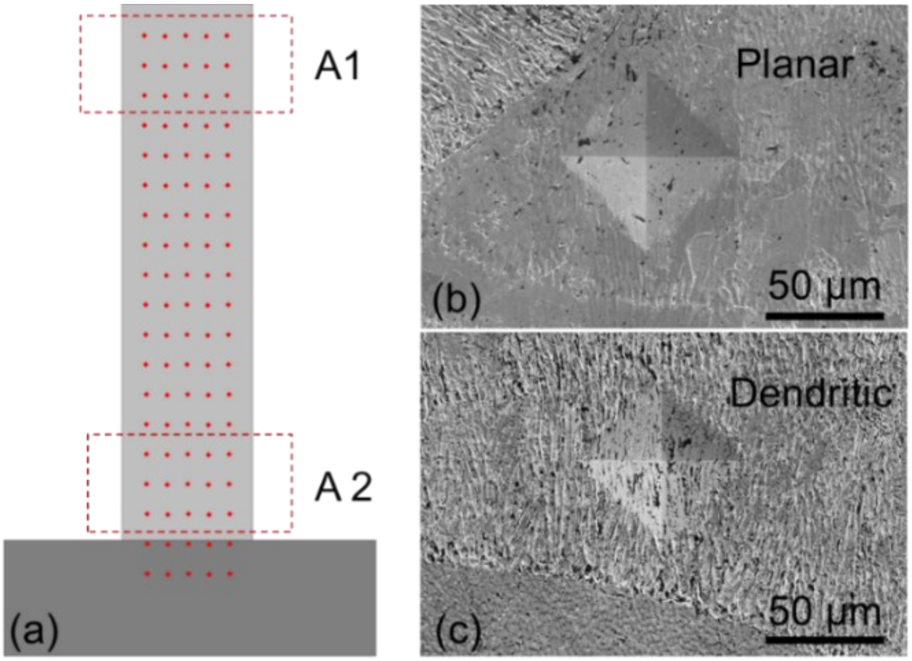

Figure 31: Illustration of variation in the microhardness resulting from different grain morphologies. (a) schematic representation of the cross-sectional view of the build, where A1 and A2 represent the top and bottom areas of the build where indents were made on dendritic and planar grain regions of an open-loop processed part. (b) and (c) SEM images of the indents made on planar and dendritic regions, respectively. Measurements from the same region are compared to show the morphology-related variation in the microhardness with results shown in Table 4.

Table 4: Comparison between the microhardness measurements performed on different microstructure morphologies from areas A1 and A2 shown in Figure 31.

	Vickers Hardness ($HV_{0.5}$)	
Region	Planar	Dendritic
A1	139 (7)	165 (5)
A2	182 (7)	202 (5)

Conclusions

In this work we achieved closed-loop control of meltpool temperature in directed energy deposition (DED). An Optomec MR7 DED machine was integrated with a two-wavelength imaging pyrometer coaxial to the laser path to measure the meltpool temperature. The meltpool temperature was maintained at a setpoint of 1650 ± 50°C through real-time modulation of the laser power using a rule-based controller.

We demonstrated the advantage of closed-loop control approach with trapezoid-shaped parts (stainless steel 316L) consisting of 198 layers with 4 hatches per layer (49.5 mm tall). Processing under closed-loop control of meltpool temperature mitigated heterogeneity in microstructure and reduced variation in porosity and microhardness compared to parts produced under open-loop conditions with fixed processing parameters. Specific conclusions are as follows.

(1) Non-destructive analysis using X-ray computed tomography revealed a large variation in porosity for open-loop processed parts – the volume percent porosity ranges from 0.032% to 0.068%. In contrast, for closed-loop processed parts, the porosity is tightly controlled in the range of 0.036% to 0.043%. A vast majority of pores (80% to 85%) were located on the contour hatches.

(2) Scanning electron microscopy revealed that parts deposited with closed-loop processing depict a homogenous dendritic microstructure across all layers and hatches. In contrast,

parts built under open-loop processing showed heterogeneous microstructure consisting of dendritic and irregular planar grains. Microstructure heterogeneity of the open-loop processed parts translated into larger variation in microhardness both between parts and within the same part. This heterogeneity of microstructure and microhardness is correlated to non-uniformity of meltpool temperature and shape.

(3) X-ray diffraction (XRD) studies showed that parts produced under closed-loop processing conditions do not result in new material phases compared to open-loop processing that could negatively affect their mechanical properties. Likewise, energy dispersive X-ray spectroscopy (EDS) affirmed that there is no difference in the material composition between parts resulting from closed-loop and open-loop processing.

The reduction in microstructure heterogeneity and flaw formation via closed-loop process control is the critical first-step towards the mitigation of uncertainty in mechanical properties of DED-processed parts. An important implication of this work is that for closed-loop meltpool control of temperature to be effective, especially in multi-hatch builds, the laser power must be modulated both hatch-by-hatch and layer-by-layer.

Data Availability Statement

The data that support the findings of this study are available by contacting Stratonics, Inc. Restrictions apply to the availability of these data, which were used under license for this study. Data are available with the permission of Dr. James Craig (email: jcraig@stratonics.com).

Acknowledgements

The DED in situ process monitoring and feedback control project was conducted under a Stratonics lead Defense Logistics Agency SBIR Phase 2, *Implementation of Thermal Sensing Controls in Additive Manufacturing for Part Quality and Process Repeatability*, Contract No. SP4701-17-C-00030 (Program Technical Point of Contact: Vaibhav Jain). The authors gratefully acknowledge the unique and skilled efforts of Benjamin Long and Lucas Brewer, Optomec NM, who made significant contributions in experiments and facilitating interface between the DED machine and pyrometer, respectively.

Prahalada Rao thanks the National Science Foundation (NSF) and Department of Energy (DoE) for funding his work under awards OIA-1929172, CMMI-1920245, CMMI-1739696, ECCS-2020246, PFI-TT 2044710, CMMI-1752069, CMMI-1719388, and DE-SC0021136. Understanding the causal influence of process parameters on part quality and detection of defect formation using in-situ sensing was the major aspect of CMMI-1752069 (Program Officer: Kevin Chou). Supplemental funding for CMMI-1752069 was obtained through the NSF INTERN program (Program Officer: Prakash Balan) and CMMI Data Science Activities (Program Officer: Martha Dodson) is greatly appreciated. The later supplement funded Ziyad Smoqi and Aniruddha Gaikwad's research. Ben Bevans' work was funded partially through the DoE Grant DE-SC0021136.

Jeffrey Shield thanks the DoE for funding this work through DE-SC0021136 (Program officer: Timothy Fitzsimmons). The materials characterization research was performed in part in the Nebraska Nanoscale Facility: National Nanotechnology Coordinated Infrastructure under award no. ECCS: 2025298, and with support from the Nebraska Research Initiative through the Nebraska Center for Materials and Nanoscience and the Nanoengineering Research Core Facility at the University of Nebraska-Lincoln. The authors gratefully acknowledge the initial XCT results provided by Mr. Scott Halliday at Navajo Technical University (NTU).

Appendix

The microhardness readings for the six parts, along with the one standard deviation. At each location five microhardness readings were recorded.

	Closed-loop processing			Open-loop processing		
Section	C1	C2	C3	O1	O2	O3
8 (43.3-49.5 mm)	165±15.4	155±13.0	162±13.2	160±16.3	154±15.5	161±18.3
7 (37.1-43.3 mm)	162±13.1	162±12.3	170±11.2	166±15.5	159±13.9	172±8.4
6 (30.9-37.1 mm)	160±11.6	158±12.5	174±11.1	180±18.8	155±14.6	183±14.6
5 (24.7-30.9 mm)	163±12.0	165±11.9	172±8.8	182±20.4	163±10.4	188±40.3
4 (18.5-24.7 mm)	182±11.6	175±14.5	169±9.2	174±25.1	162±19.1	170±14.6
3 (12.3-18.5 mm)	186±10.7	183±14.0	174±11.7	183±22.8	166±7.5	174±15.7
2 (6.2-12.3 mm)	198±14.2	184±11.7	183±11.9	184±13.9	167±11.9	179±15.5
1 (0.00-6.2 mm)	222±14.5	192±11.0	193±11.7	192±13.0	182±10.3	183±11.7

References

[1] A. Dass, A. Moridi, State of the art in directed energy deposition: From additive manufacturing to materials design, Coatings 9(7) (2019) 418. https://doi.org/10.3390/coatings9070418

[2] J.S. Panchagnula, S. Simhambhatla, Manufacture of complex thin-walled metallic objects using weld-deposition based additive manufacturing, Robotics and Computer-Integrated Manufacturing 49 (2018) 194-203. https://doi.org/10.1016/j.rcim.2017.06.003

[3] Z. Smoqi, J. Toddy, H. Halliday, J.E. Shield, P. Rao, Process-structure relationship in the directed energy deposition of cobalt-chromium alloy (Stellite 21) coatings, Materials & Design 197 (2021) 109229. https://doi.org/10.1016/j.matdes.2020.109229

[4] A. Saboori, A. Aversa, G. Marchese, S. Biamino, M. Lombardi, P. Fino, Application of directed energy deposition-based additive manufacturing in repair, Applied Sciences 9(16) (2019) 3316. https://doi.org/10.3390/app9163316

[5] M. Montazeri, A.R. Nassar, C.B. Stutzman, P. Rao, Heterogeneous sensor-based condition monitoring in directed energy deposition, Additive Manufacturing 30 (2019) 100916. https://doi.org/10.1016/j.addma.2019.100916

[6] S. Wolff, T. Lee, E. Faierson, K. Ehmann, J. Cao, Anisotropic properties of directed energy deposition (DED)-processed Ti–6Al–4V, Journal of Manufacturing Processes 24 (2016) 397-405. https://doi.org/10.1016/j.jmapro.2016.06.020

[7] B.E. Carroll, T.A. Palmer, A.M. Beese, Anisotropic tensile behavior of Ti–6Al–4V components fabricated with directed energy deposition additive manufacturing, Acta Materialia 87 (2015) 309-320. https://doi.org/10.1016/j.actamat.2014.12.054

[8] Z.-j. Tang, W.-w. Liu, Y.-w. Wang, K.M. Saleheen, Z.-c. Liu, S.-t. Peng, Z. Zhang, H.-c. Zhang, A review on in situ monitoring technology for directed energy deposition of metals, The International Journal of Advanced Manufacturing Technology 108(11) (2020) 3437-3463. https://doi.org/10.1007/s00170-020-05569-3

[9] J.L. Dávila, P.I. Neto, P.Y. Noritomi, R.T. Coelho, J.V.L. da Silva, Hybrid manufacturing: a review of the synergy between directed energy deposition and subtractive processes, The International Journal of Advanced Manufacturing Technology 110(11) (2020) 3377-3390. https://doi.org/10.1007/s00170-020-06062-7

[10] Z. Yan, W. Liu, Z. Tang, X. Liu, N. Zhang, M. Li, H. Zhang, Review on thermal analysis in laser-based additive manufacturing, Optics & Laser Technology 106 (2018) 427-441. https://doi.org/10.1016/j.optlastec.2018.04.034

[11] D.S. Ertay, M.A. Naiel, M. Vlasea, P. Fieguth, Process performance evaluation and classification via in-situ melt pool monitoring in directed energy deposition, CIRP Journal of Manufacturing Science and Technology 35 (2021) 298-314. https://doi.org/10.1016/j.cirpj.2021.06.015

[12] L.E. dos Santos Paes, M. Pereira, F.A. Xavier, W.L. Weingaertner, L.O. Vilarinho, Lack of fusion mitigation in directed energy deposition with laser (DED-L) additive manufacturing through laser remelting, Journal of Manufacturing Processes 73 (2022) 67-77. https://doi.org/10.1016/j.jmapro.2021.10.052

[13] A. Gaikwad, R. Yavari, M. Montazeri, K. Cole, L. Bian, P. Rao, Toward the digital twin of additive manufacturing: Integrating thermal simulations, sensing, and analytics to detect process faults, IISE Transactions 52(11) (2020) 1204-1217. https://doi.org/10.1080/24725854.2019.1701753

[14] L. Xu, Y. Gao, L. Zhao, Y. Han, H. Jing, Ultrasonic micro-forging post-treatment assisted laser directed energy deposition approach to manufacture high-strength Hastelloy X superalloy, Journal of Materials Processing Technology 299 (2022) 117324. https://doi.org/10.1016/j.jmatprotec.2021.117324

[15] B. Zheng, J.C. Haley, N. Yang, J. Yee, K.W. Terrassa, Y. Zhou, E.J. Lavernia, J.M. Schoenung, On the evolution of microstructure and defect control in 316L SS components fabricated via directed energy deposition, Materials Science and Engineering: A 764 (2019) 138243. https://doi.org/10.1016/j.msea.2019.138243

[16] Q. Yang, P. Zhang, L. Cheng, Z. Min, M. Chyu, A.C. To, Finite element modeling and validation of thermomechanical behavior of Ti-6Al-4V in directed energy deposition additive manufacturing, Additive Manufacturing 12 (2016) 169-177. https://doi.org/10.1016/j.addma.2016.06.012

[17] B. Bax, R. Rajput, R. Kellet, M. Reisacher, Systematic evaluation of process parameter maps for laser cladding and directed energy deposition, Additive Manufacturing 21 (2018) 487-494. https://doi.org/10.1016/j.addma.2018.04.002

[18] N. Shamsaei, A. Yadollahi, L. Bian, S.M. Thompson, An overview of Direct Laser Deposition for additive manufacturing; Part II: Mechanical behavior, process parameter optimization and control, Additive Manufacturing 8 (2015) 12-35. https://doi.org/10.1016/j.addma.2015.07.002

[19] J.S. Keist, T.A. Palmer, Role of geometry on properties of additively manufactured Ti-6Al-4V structures fabricated using laser based directed energy deposition, Materials & Design 106 (2016) 482-494. https://doi.org/10.1016/j.matdes.2016.05.045

[20] J.P. Oliveira, T.G. Santos, R.M. Miranda, Revisiting fundamental welding concepts to improve additive manufacturing: From theory to practice, Progress in Materials Science 107 (2020) 100590. https://doi.org/10.1016/j.pmatsci.2019.100590

[21] J.C. Haley, J.M. Schoenung, E.J. Lavernia, Modelling particle impact on the melt pool and wettability effects in laser directed energy deposition additive manufacturing, Materials Science and Engineering: A 761 (2019) 138052. https://doi.org/10.1016/j.msea.2019.138052

[22] S.M. Thompson, L. Bian, N. Shamsaei, A. Yadollahi, An overview of Direct Laser Deposition for additive manufacturing; Part I: Transport phenomena, modeling and diagnostics, Additive Manufacturing 8 (2015) 36-62. https://doi.org/10.1016/j.addma.2015.07.001

[23] M. Seifi, M. Gorelik, J. Waller, N. Hrabe, N. Shamsaei, S. Daniewicz, J.J. Lewandowski, Progress towards metal additive manufacturing standardization to support qualification and certification, Jom 69(3) (2017) 439-455. https://doi.org/10.1007/s11837-017-2265-2

[24] A. Singh, S. Kapil, M. Das, A comprehensive review of the methods and mechanisms for powder feedstock handling in directed energy deposition, Additive Manufacturing 35 (2020) 101388. https://doi.org/10.1016/j.addma.2020.101388

[25] M. Liu, A. Kumar, S. Bukkapatnam, M. Kuttolamadom, A Review of the Anomalies in Directed Energy Deposition (DED) Processes & Potential Solutions - Part Quality & Defects, Procedia Manufacturing 53 (2021) 507-518. https://doi.org/10.1016/j.promfg.2021.06.093

[26] V. Errico, S.L. Campanelli, A. Angelastro, M. Dassisti, M. Mazzarisi, C. Bonserio, Coaxial Monitoring of AISI 316L Thin Walls Fabricated by Direct Metal Laser Deposition, Materials 14(3) (2021) 673. https://doi.org/10.3390/ma14030673

[27] C. Kledwig, H. Perfahl, M. Reisacher, F. Brückner, J. Bliedtner, C. Leyens, Analysis of Melt Pool Characteristics and Process Parameters Using a Coaxial Monitoring System during Directed Energy Deposition in Additive Manufacturing, Materials 12(2) (2019) 308. https://doi.org/10.3390/ma12020308

[28] M. Akbari, R. Kovacevic, Closed loop control of melt pool width in robotized laser powder–directed energy deposition process, The International Journal of Advanced Manufacturing Technology 104(5) (2019) 2887-2898. https://doi.org/10.1007/s00170-019-04195-y

[29] M.H. Farshidianfar, F. Khodabakhshi, A. Khajepour, A.P. Gerlich, Closed-loop control of microstructure and mechanical properties in additive manufacturing by directed energy deposition, Materials Science and Engineering: A (2020) 140483. https://doi.org/10.1016/j.msea.2020.140483

[30] E.W. Reutzel, A.R. Nassar, A survey of sensing and control systems for machine and process monitoring of directed-energy, metal-based additive manufacturing, Rapid Prototyping Journal 21(2) (2015) 159-167. https://doi.org/10.1108/RPJ-12-2014-0177

[31] H. Wang, W. Liu, Z. Tang, Y. Wang, X. Mei, K. Saleheen, Z. Wang, H. Zhang, Review on adaptive control of laser-directed energy deposition, Optical Engineering 59(7) (2020) 070901. https://doi.org/10.1117/1.OE.59.7.070901

[32] L. Song, V. Bagavath-Singh, B. Dutta, J. Mazumder, Control of melt pool temperature and deposition height during direct metal deposition process, The International Journal of Advanced Manufacturing Technology 58(1) (2012) 247-256. https://doi.org/10.1007/s00170-011-3395-2

[33] L. Tang, R.G. Landers, Melt Pool Temperature Control for Laser Metal Deposition Processes—Part II: Layer-to-Layer Temperature Control, Journal of Manufacturing Science and Engineering 132(1) (2010). https://doi.org/10.1115/1.4000883

[34] Optomec, PROCESS MONITORING AND CONTROLS, 2018. https://www.optomec.com/wp-content/uploads/2014/04/LENS_process-monitor-controls_datasheet.pdf.

[35] M. Khanzadeh, W. Tian, A. Yadollahi, H.R. Doude, M.A. Tschopp, L. Bian, Dual process monitoring of metal-based additive manufacturing using tensor decomposition of thermal image streams, Additive Manufacturing 23 (2018) 443-456. https://doi.org/10.1016/j.addma.2018.08.014

[36] P.A. Hooper, Melt pool temperature and cooling rates in laser powder bed fusion, Additive Manufacturing 22 (2018) 548-559. https://doi.org/10.1016/j.addma.2018.05.032

[37] J.A. Mitchell, T.A. Ivanoff, D. Dagel, J.D. Madison, B. Jared, Linking pyrometry to porosity in additively manufactured metals, Additive Manufacturing 31 (2020) 100946. https://doi.org/10.1016/j.addma.2019.100946

[38] D. Salehi, M. Brandt, Melt pool temperature control using LabVIEW in Nd:YAG laser blown powder cladding process, The International Journal of Advanced Manufacturing Technology 29(3) (2006) 273-278. https://doi.org/10.1007/s00170-005-2514-3

[39] A.R. Nassar, J.S. Keist, E.W. Reutzel, T.J. Spurgeon, Intra-layer closed-loop control of build plan during directed energy additive manufacturing of Ti–6Al–4V, Additive Manufacturing 6 (2015) 39-52. https://doi.org/10.1016/j.addma.2015.03.005

[40] L. Tang, R.G. Landers, Melt Pool Temperature Control for Laser Metal Deposition Processes—Part I: Online Temperature Control, Journal of Manufacturing Science and Engineering 132(1) (2010). https://doi.org/10.1115/1.4000882

[41] B.T. Gibson, Y.K. Bandari, B.S. Richardson, W.C. Henry, E.J. Vetland, T.W. Sundermann, L.J. Love, Melt pool size control through multiple closed-loop modalities in laser-wire directed energy deposition of Ti-6Al-4V, Additive Manufacturing 32 (2020) 100993. https://doi.org/10.1016/j.addma.2019.100993

[42] D. Becker, S. Boley, R. Eisseler, T. Stehle, H.-C. Möhring, V. Onuseit, M. Hoßfeld, T. Graf, Influence of a closed-loop controlled laser metal wire deposition process of S Al 5356 on the quality of manufactured parts before and after subsequent machining, Production Engineering 15(3) (2021) 489-507. https://doi.org/10.1007/s11740-021-01030-w

[43] M.H. Farshidianfar, A. Khajepour, A. Gerlich, Real-time control of microstructure in laser additive manufacturing, The International Journal of Advanced Manufacturing Technology 82(5-8) (2016) 1173-1186. https://doi.org/10.1007/s00170-015-7423-5

[44] L. Wang, S.D. Felicelli, J.E. Craig, Thermal modeling and experimental validation in the LENS™ process, 2007 International Solid Freeform Fabrication Symposium (2007). http://dx.doi.org/10.26153/tsw/7197

[45] S.K. Everton, M. Hirsch, P. Stravroulakis, R.K. Leach, A.T. Clare, Review of in-situ process monitoring and in-situ metrology for metal additive manufacturing, Materials & Design 95 (2016) 431-445. https://doi.org/10.1016/j.matdes.2016.01.099

[46] S. Moylan, E. Whitenton, B. Lane, J. Slotwinski, Infrared thermography for laser-based powder bed fusion additive manufacturing processes, AIP Conference Proceedings 1581(1) (2014) 1191-1196. https://doi.org/10.1063/1.4864956

[47] B. Lane, L. Jacquemetton, M. Piltch, D. Beckett, Thermal Calibration of Commercial Melt Pool Monitoring Sensors on a Laser Powder Bed Fusion System, National Institute of Standards and Technology (NIST), Advanced Manufacturing Series. Series 100-35 (2020). https://doi.org/10.6028/NIST.AMS.100-35

[48] J.C. Heigel, P. Michaleris, T.A. Palmer, Measurement of forced surface convection in directed energy deposition additive manufacturing, Proceedings of the Institution of Mechanical Engineers, Part B: Journal of Engineering Manufacture 230(7) (2015) 1295-1308. https://doi.org/10.1177/0954405415599928

[49] N.A. Kistler, D.J. Corbin, A.R. Nassar, E.W. Reutzel, A.M. Beese, Effect of processing conditions on the microstructure, porosity, and mechanical properties of Ti-6Al-4V repair fabricated by directed energy deposition, Journal of Materials Processing Technology 264 (2019) 172-181. https://doi.org/10.1016/j.jmatprotec.2018.08.041

[50] M. Akbari, R. Kovacevic, An investigation on mechanical and microstructural properties of 316LSi parts fabricated by a robotized laser/wire direct metal deposition system, Additive Manufacturing 23 (2018) 487-497. https://doi.org/10.1016/j.addma.2018.08.031

[51] N. Yang, J. Yee, B. Zheng, K. Gaiser, T. Reynolds, L. Clemon, W.Y. Lu, J.M. Schoenung, E.J. Lavernia, Process-Structure-Property Relationships for 316L Stainless Steel Fabricated by Additive Manufacturing and Its Implication for Component Engineering, Journal of Thermal Spray Technology 26(4) (2017) 610-626. https://doi.org/10.1007/s11666-016-0480-y

[52] K. Weman, 19 - The weldability of steel, in: K. Weman (Ed.), Welding Processes Handbook (Second Edition), Woodhead Publishing2012, pp. 191-206. https://doi.org/10.1533/9780857095183.191

[53] F. Lia, J.Z. Park, J.S. Keist, S. Joshi, R.P. Martukanitz, Thermal and microstructural analysis of laser-based directed energy deposition for Ti-6Al-4V and Inconel 625 deposits, Materials Science and Engineering: A 717 (2018) 1-10. https://doi.org/10.1016/j.msea.2018.01.060

[54] J. Elmer, S. Allen, T. Eagar, Microstructural development during solidification of stainless steel alloys, Metallurgical transactions A 20(10) (1989) 2117-2131. https://doi.org/10.1007/BF02650298

[55] S. Katayama, A. Matsunawa, Solidification microstructure of laser welded stainless steels, International Congress on Applications of Lasers & Electro-Optics 1984(2) (1984) 60-67. https://doi.org/10.2351/1.5057623

[56] D. Galicki, B.C. Chakoumakos, S.P. Ringer, M. Eizadjou, C.J. Rawn, K. Nomoto, S.S. Babu, On the formation of spherical metastable BCC single crystal spatter particles during laser powder bed fusion, Materialia 9 (2020) 100584. https://doi.org/10.1016/j.mtla.2020.100584

[57] A. Matsunawa, S. Katayama, Fusion and solidification processes of pulsed YAG laser spot welds, International Congress on Applications of Lasers & Electro-Optics 1986(S2) (1986) 81-87. https://doi.org/10.2351/1.5057872

[58] T. Lienert, T. Siewert, S. Babu, V. Acoff, S.W.P. Specifications, ASM handbook, volume 6A: welding fundamentals and processes, ASM International Materials Park, OH2011.

[59] F. Yan, W. Xiong, E.J. Faierson, Grain structure control of additively manufactured metallic materials, Materials 10(11) (2017) 1260. https://doi.org/10.3390/ma10111260

[60] S. Kou, Welding metallurgy, New Jersey, USA (2003) 431-446. https://doi.org/10.1557/mrs2003.197

[61] H. Wei, J. Mazumder, T. DebRoy, Evolution of solidification texture during additive manufacturing, Scientific reports 5 (2015) 16446. https://doi.org/10.1038/srep16446

[62] K. Zhang, S. Wang, W. Liu, X. Shang, Characterization of stainless steel parts by Laser Metal Deposition Shaping, Materials & Design 55 (2014) 104-119. https://doi.org/10.1016/j.matdes.2013.09.006

[63] Y. Zhong, L. Liu, S. Wikman, D. Cui, Z. Shen, Intragranular cellular segregation network structure strengthening 316L stainless steel prepared by selective laser melting, Journal of Nuclear Materials 470 (2016) 170-178. https://doi.org/10.1016/j.jnucmat.2015.12.034

[64] Y. Zhong, L.-E. Rännar, L. Liu, A. Koptyug, S. Wikman, J. Olsen, D. Cui, Z. Shen, Additive manufacturing of 316L stainless steel by electron beam melting for nuclear fusion applications, Journal of Nuclear Materials 486 (2017) 234-245. https://doi.org/10.1016/j.jnucmat.2016.12.042

[65] Q. Wang, S. Zhang, C. Zhang, C. Wu, J. Wang, J. Chen, Z. Sun, Microstructure evolution and EBSD analysis of a graded steel fabricated by laser additive manufacturing, Vacuum 141 (2017) 68-81. https://doi.org/10.1016/j.vacuum.2017.03.021

[66] M.S.F. de Lima, S. Sankaré, Microstructure and mechanical behavior of laser additive manufactured AISI 316 stainless steel stringers, Materials & Design 55 (2014) 526-532. https://doi.org/10.1016/j.matdes.2013.10.016

[67] P. Ganesh, R. Giri, R. Kaul, P. Ram Sankar, P. Tiwari, A. Atulkar, R.K. Porwal, R.K. Dayal, L.M. Kukreja, Studies on pitting corrosion and sensitization in laser rapid manufactured specimens of type 316L stainless steel, Materials & Design 39 (2012) 509-521. https://doi.org/10.1016/j.matdes.2012.03.011

[68] F. Weng, S. Gao, J. Jiang, J. Wang, P. Guo, A novel strategy to fabricate thin 316L stainless steel rods by continuous directed energy deposition in Z direction, Additive Manufacturing 27 (2019) 474-481. https://doi.org/10.1016/j.addma.2019.03.024

[69] P. Guo, B. Zou, C. Huang, H. Gao, Study on microstructure, mechanical properties and machinability of efficiently additive manufactured AISI 316L stainless steel by high-power direct laser deposition, Journal of Materials Processing Technology 240 (2017) 12-22. https://doi.org/10.1016/j.jmatprotec.2016.09.005

[70] T. Wegrzyn, Delta ferrite in stainless steel weld metals, Welding International 6(9) (1992) 690-694. https://doi.org/10.1080/09507119209548267

[71] M. Ziętala, T. Durejko, M. Polański, I. Kunce, T. Płociński, W. Zieliński, M. Łazińska, W. Stępniowski, T. Czujko, K.J. Kurzydłowski, Z. Bojar, The microstructure, mechanical properties and corrosion resistance of 316L stainless steel fabricated using laser engineered net shaping, Materials Science and Engineering: A 677 (2016) 1-10. https://doi.org/10.1016/j.msea.2016.09.028